

Quantum critical properties of a metallic spin-density-wave transition

Max H. Gerlach,¹ Yoni Schattner,² Erez Berg,² and Simon Trebst¹

¹*Institute for Theoretical Physics, University of Cologne, 50937 Cologne, Germany*

²*Department of Condensed Matter Physics, The Weizmann Institute of Science, Rehovot, 76100, Israel*

(Received 4 October 2016; published 17 January 2017)

We report on numerically exact determinantal quantum Monte Carlo simulations of the onset of spin-density-wave (SDW) order in itinerant electron systems captured by a sign-problem-free two-dimensional lattice model. Extensive measurements of the SDW correlations in the vicinity of the phase transition reveal that the critical dynamics of the bosonic order parameter are well described by a dynamical critical exponent $z = 2$, consistent with Hertz-Millis theory, but are found to follow a finite-temperature dependence that does not fit the predicted behavior of the same theory. The presence of critical SDW fluctuations is found to have a strong impact on the fermionic quasiparticles, giving rise to a dome-shaped superconducting phase near the quantum critical point. In the superconducting state we find a gap function that has an opposite sign between the two bands of the model and is nearly constant along the Fermi surface of each band. Above the superconducting T_c , our numerical simulations reveal a nearly temperature and frequency independent self-energy causing a strong suppression of the low-energy quasiparticle weight in the vicinity of the hot spots on the Fermi surface. This indicates a clear breakdown of Fermi liquid theory around these points.

DOI: [10.1103/PhysRevB.95.035124](https://doi.org/10.1103/PhysRevB.95.035124)

I. INTRODUCTION

Metallic spin-density-wave (SDW) transitions are ubiquitous to strongly correlated materials such as the electron-doped cuprates [1], the Fe-based superconductors [2], heavy fermion systems [3], and organic superconductors [4]. In all these materials, unconventional superconductivity is found to emerge near the onset of SDW order, with the maximum of the superconducting T_c occurring either at or near the underlying SDW quantum phase transition (QPT). In addition, the vicinity of the SDW transition is often characterized by strong deviations from Fermi liquid theory—both in thermodynamic and in single electron properties.

More broadly, understanding the properties of quantum critical points (QCPs) in itinerant fermion systems has attracted much interest over the past several decades [5–29]. Unlike thermal critical phenomena and QCPs in insulating systems, here the critical order parameter fluctuations are strongly interacting with low-energy fermionic quasiparticles near the Fermi surface. In the traditional approach to this problem due to Hertz [5], later refined by Millis [6], the fermions are integrated out from the outset, leading to an effective *bosonic* action for the order parameter fluctuations. The dynamics of the order parameter is found to be overdamped due to the coupling to the fermions, that act as a bath. The effective bosonic action is then treated using conventional renormalization group (RG) techniques. While physically appealing, this approach has the drawback that integrating out low-energy modes is dangerous, since it generates nonanalytic terms in momentum and frequency that are difficult to treat within the RG scheme. An alternative popular approach has been to use a $1/N$ expansion [8], where N is the number of fermion flavors. However, in the important case of two spatial dimensions, this approach turns out to be uncontrolled, as well [12,15]. Alternative expansion parameters have been introduced in order to control the problem [13,18], or have been proposed to emerge naturally [29]. A fully controlled analytical treatment of QCPs in itinerant electron systems has remained one of the grand challenges in strongly correlated electron physics.

In addition to the bosonic critical fluctuation dynamics, an important open question regards the behavior of the *fermionic* quasiparticles in the vicinity of the transition. The exchange of SDW critical fluctuations can mediate a superconducting instability; however, the same fluctuations also strongly scatter the quasiparticles, causing them to lose their coherence and leading to the formation of a non-Fermi liquid metal. It is not clear which of these effects dominates, i.e., is there a well-defined non-Fermi liquid regime that precedes superconductivity, or does pairing always preempt the formation of a non-Fermi liquid [30]?

In this work, we perform extensive numerically exact determinantal quantum Monte Carlo (QMC) simulations [31–35] of a metallic system in the vicinity of an SDW transition. We use the approach of Refs. [17,28], that introduced a two-dimensional multiband lattice model that captures the generic structure of the “hot spots”—points on the Fermi surface where quasiparticles can scatter off critical SDW fluctuations resonantly. The universal properties of metallic SDW transitions are believed to depend only on the vicinity of the hot spots. At the same time, the model is amenable to QMC simulations without a sign problem [17]. Our goal here is both to understand the generic properties of the transition, and to provide a controlled benchmark to analytic theories. We present detailed information about the bosonic and fermionic correlations and the interplay with unconventional superconductivity in the vicinity of the QCP.

Previously, the finite-temperature phase diagram of the model has been characterized, and a dome-shaped superconducting phase peaked near the SDW transition was found [28,36]. Here, we measure the SDW correlations in the vicinity of the transition, above the superconducting T_c . We find that, over a broad range of parameters, the SDW susceptibility is well described by the following form:

$$\chi_0(\mathbf{q}, \omega_n, r, T) = \frac{1}{a_q(\mathbf{q} - \mathbf{Q})^2 + a_\omega|\omega_n| + a_r(r - r_c) + f(r, T)}. \quad (1)$$

Here, \mathbf{Q} is the ordering wave vector [chosen to be (π, π) in our model], $\omega_n = 2\pi nT$ is a Matsubara frequency, and r is a parameter used for tuning through the SDW QCP, while a_q , a_ω , a_r , and r_{c0} are nonuniversal constants. The function $f(r, T)$ extrapolates to 0 as $T \rightarrow 0$. Importantly, Eq. (1) captures the behavior of both the bosonic SDW correlations and the susceptibility of a fermion bilinear operator with the same symmetry, establishing the consistency of our analysis.

Interestingly, $\chi_0(\mathbf{q}, \omega_n, r, T \rightarrow 0)$ has precisely the form predicted by Hertz and Millis; in particular, the bosonic critical dynamics are characterized by a dynamic critical exponent $z = 2$. The function $f(r, T)$ does not follow the predicted behavior, however. In a window of temperatures above T_c , we find a power-law dependence $f(r \approx r_{c0}, T) \propto T^\alpha$ with $\alpha \simeq 2$, in contrast to the linear behavior predicted by Millis [6,37].

The single-fermion properties above T_c are found to depend strongly on the distance from the hot spots. Away from the hot spots, a behavior consistent with Fermi liquid theory is observed. At the hot spots, a substantial loss of spectral weight is seen upon approaching the QCP. In a temperature window above T_c , the fermionic self-energy is only weakly frequency and temperature dependent, corresponding to a nearly-constant lifetime of quasiparticles at the hot spots. This behavior indicates a strong breakdown of Fermi liquid theory at these points. It is not clear, however, whether it represents the asymptotic behavior at the putative underlying SDW QCP, since superconductivity intervenes before the QCP is reached.

Finally, in order to probe the interplay between magnetic quantum criticality and superconductivity, we measure the superconducting gap, $\Delta_{\mathbf{k}}$, and the momentum-resolved superconducting susceptibility, $P_{\mathbf{k}, \mathbf{k}'}$, across the phase diagram. No strong feature is found in $\Delta_{\mathbf{k}}$ at the hot spots. Rather, $\Delta_{\mathbf{k}}$ and $P_{\mathbf{k}, \mathbf{k}'}$ vary smoothly on the Fermi surface. While the pairing interaction may be strongly peaked at wave vector \mathbf{Q} , the resulting gap function does not reflect such a strong momentum dependence.

This paper is organized as follows. In Sec. II, we describe the model and review its phase diagram. Section III presents a detailed analysis of the SDW susceptibility across the phase diagram. In Sec. IV, we study the single-fermion properties, providing evidence for the breakdown of Fermi liquid theory in the vicinity of the hot spots. Section V analyzes the gap structure in the superconducting state. The cumulative results are put into perspective in Sec. VI. Supplementary data sets and some technical details are presented in the appendices.

II. THE MODEL AND THE PHASE DIAGRAM

Our lattice model is composed of two flavors of spin- $\frac{1}{2}$ fermions, ψ_x and ψ_y , that are coupled to a real bosonic vector field $\vec{\varphi}$, which represents fluctuations of a commensurate SDW order parameter at wave vector $\mathbf{Q} = (\pi, \pi)$. The two types of fermions exhibit quasi one-dimensional dispersions along momenta k_x and k_y , respectively, which in the absence of interactions give rise to the Fermi surfaces illustrated in Fig. 1. It is precisely this two-flavor structure that fundamentally allows us to set up an action completely devoid of the fermion sign problem in QMC simulations [17]. Yet, the Fermi surfaces of this model capture the generic structure of the hot spots,

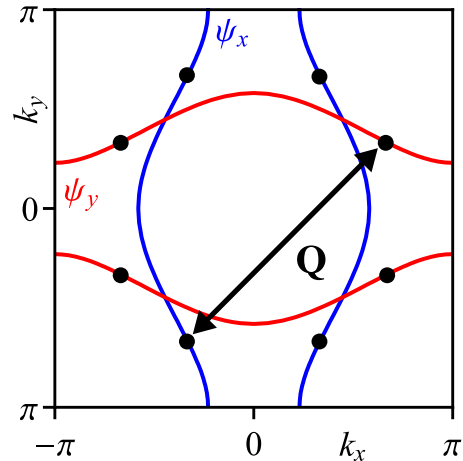


FIG. 1. Noninteracting Fermi surfaces of the ψ_x and ψ_y fermions. Hot spots (indicated by the black dots) are linked by the vector $\mathbf{Q} = (\pi, \pi)$ with points on the other band. The ψ_x and ψ_y fermions have stronger dispersion in direction k_x and k_y , respectively.

which is generally believed to determine the universal physics near the QCP.

As in our previous work on this model [28], we assume an $O(2)$ symmetric SDW order parameter, i.e., $\vec{\varphi}$ is restricted to the XY plane. In contrast to the case of an $O(3)$ order parameter (studied in Refs. [17,36]), the easy-plane order parameter implies the existence of a *finite-temperature* SDW phase transition of Berezinskii-Kosterlitz-Thouless (BKT) character, which we can track in our numerics. In addition, the reduced dimensionality of the order parameter brings a welcome computational benefit as it enables a reduction of the dimensions of all single-fermion matrices by half, greatly improving the efficiency of the numerical linear algebra.

Our lattice model is given by the action $S = S_F + S_\varphi = \int_0^\beta d\tau (L_F + L_\varphi)$ with¹

$$\begin{aligned}
 L_F &= \sum_{\substack{i,j,s \\ \alpha=x,y}} \psi_{i\alpha s}^\dagger [(\partial_\tau - \mu)\delta_{ij} - t_{\alpha ij}] \psi_{j\alpha s} \\
 &\quad + \lambda \sum_{i,s,s'} [\vec{s} \cdot \vec{\varphi}_i]_{ss'} \psi_{ixs}^\dagger \psi_{iys'} + \text{H.c.}, \\
 L_\varphi &= \frac{1}{2} \sum_i \frac{1}{c^2} \left(\frac{d\vec{\varphi}_i}{d\tau} \right)^2 + \frac{1}{2} \sum_{\langle i,j \rangle} (e^{i\mathbf{Q}\cdot\mathbf{r}_i} \vec{\varphi}_i - e^{i\mathbf{Q}\cdot\mathbf{r}_j} \vec{\varphi}_j)^2 \\
 &\quad + \sum_i \left[\frac{r}{2} \vec{\varphi}_i^2 + \frac{u}{4} (\vec{\varphi}_i^2)^2 \right]. \tag{2}
 \end{aligned}$$

This action is defined on a square lattice with sites labeled by $i, j = 1, \dots, N_s$, where $\langle i, j \rangle$ are nearest neighbors. The two fermion flavors are indexed by $\alpha = x, y$, while $s, s' = \uparrow, \downarrow$ index the spin polarizations and \vec{s} are the Pauli matrices. Imaginary time is denoted by τ and $\beta = 1/T$ is the inverse temperature. The fermionic dispersions are implemented by

¹Note a slight change in notation compared to our previous publication [28].

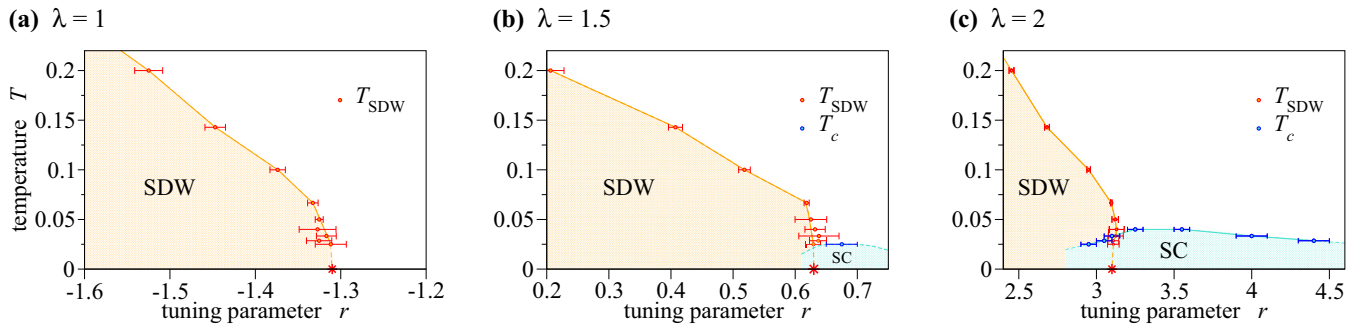


FIG. 2. Finite-temperature phase diagram of model (2) for three different values of the Yukawa coupling λ and bare bosonic velocity $c = 3$. Shown are the transition temperature T_{SDW} to magnetic spin density wave (SDW) order as well as the estimated location of the zero-temperature phase transition point r_c (indicated by the red star). The superconducting (SC) transition temperature T_c is shown where applicable. In the same units the Fermi energy is $E_F = 2.5$. Dashed lines are a guide to the eye.

setting different hopping amplitudes along the horizontal and vertical lattice directions. For the ψ_x fermions they are given by $t_{x,h} = 1$ and $t_{x,v} = 0.5$, respectively, and for the ψ_y fermions by $t_{y,h} = 0.5$ and $t_{y,v} = 1$. Note that our model is fully C_4 -symmetric with a $\pi/2$ rotation mapping the ψ_x band to the ψ_y band and vice versa. The tuning parameter r allows to tune the system to the vicinity of an SDW instability. In an experimental system, r could be proportional to a physical tuning parameter such as pressure or doping. We set the chemical potential to $\mu = -0.5$, such that the Fermi energy, measured relative to the band bottom, is $E_F = 2.5$. The quartic coupling is set to $u = 1$. The second term in L_φ favors commensurate antiferromagnetic order in $\vec{\varphi}$ with $\mathbf{Q} = (\pi, \pi)$. In the following we mostly focus on the case of a bare bosonic velocity of $c = 3$ and a Yukawa coupling between fermions and bosons of $\lambda = 1.5$. Occasionally, we also consider other values of c and λ .

Our numerical analysis of model (2) is based on extensive finite-temperature DQMC [31–35] simulations. For the general setup and technical details on the implementation of our DQMC simulations, we refer to our earlier paper [28] and its detailed supplemental online material. Here we want to single out a few conceptual aspects of our setup, which have allowed to push our simulations down to temperatures of $T = 1/40$ for system sizes up to 16×16 sites. First, using a replica-exchange scheme [38,39] in combination with a global update procedure [28] thermal equilibration of our simulations is decidedly improved. Most of our simulations were performed in the presence of a weak fictitious perpendicular “magnetic” field (designed not to break time-reversal symmetry), which serves to greatly speed up convergence to the thermodynamic limit for metallic systems [28,40,41]. Since this technique breaks translational invariance of the fermionic Green’s function, we cannot make use of it to study \mathbf{k} -resolved fermionic observables. For this reason we have carried out additional simulations without the magnetic flux, but with twisted boundary conditions, which allows to increase the momentum space resolution. We give details on these procedures in Appendix A.

To set the stage for our discussion in the following sections, we summarize the finite-temperature phase diagram of model (2) for $c = 3$ and three different values of the Yukawa coupling $\lambda = 1, 1.5, \text{ and } 2$ in Fig. 2. Besides a

paramagnetic regime for sufficiently high temperature, the dominant feature of these phase diagrams is a quasi-long-range ordered SDW phase whose transition temperature T_{SDW} is suppressed with increasing tuning parameter r . Extrapolating the SDW transition down to the zero temperature provides an estimate of the location of the quantum phase transition at $r = r_c$ (indicated by the red star). At low temperatures, the SDW transition may become weakly first order [28]. However, in the temperature range considered here, the transition is either continuous or (possibly) very weakly first order. While for $\lambda = 1$, this SDW phase is the only ordered phase down to temperatures of $T = 1/40$, there is an additional superconducting phase emerging in the vicinity of the QPT for the two larger values of the Yukawa coupling. For $\lambda = 1.5$, we barely observe the tip of this quasi-long-range ordered phase with a maximum critical temperature of $T_c^{\text{max}} \approx 1/40$, which is our numerical temperature limit. For $\lambda = 2$, we can clearly map out a superconducting dome with the maximum of the critical temperature $T_c^{\text{max}} \approx 1/20$.

At finite temperatures, both the SDW and the SC finite-temperature transitions are expected to be of BKT type. The SDW susceptibility $\chi = \int d\tau \sum_i e^{i\mathbf{Q}\cdot\mathbf{r}_i} \langle \vec{\varphi}_i(\tau) \vec{\varphi}_0(0) \rangle$ is found to follow a scaling law $\chi \propto L^{2-\eta}$ with a continuously changing exponent η . We identify the transition temperature T_{SDW} with the point where the exponent takes the universal value $\eta = 1/4$. The SC transition temperature can be both determined via a similar η fit or by the point where the superfluid density ρ_s obtains the universal value of $2T_c/\pi$. Both estimates are found to agree. The error bars in Fig. 2 are mostly due to finite-size effects. For further details on the procedures employed to identify the different phase transitions see Ref. [28] and its accompanying supplementary online material.

A common feature to all three phase diagrams is a change of slope of the SDW phase boundary curve at low temperatures ($T \approx 0.07$). This apparent “bending” is more pronounced at larger Yukawa coupling λ . Such behavior is generally expected to occur at the onset of superconductivity [28,42]. Here, however, the bending does not visibly track the SC transition temperature. The curvature of the T_{SDW} line is also reflected in the SDW susceptibility in the paramagnetic region of the phase diagram, see Fig. 3 for $\lambda = 1$ and Fig. 18 in Appendix B for $\lambda = 1.5, 2$.

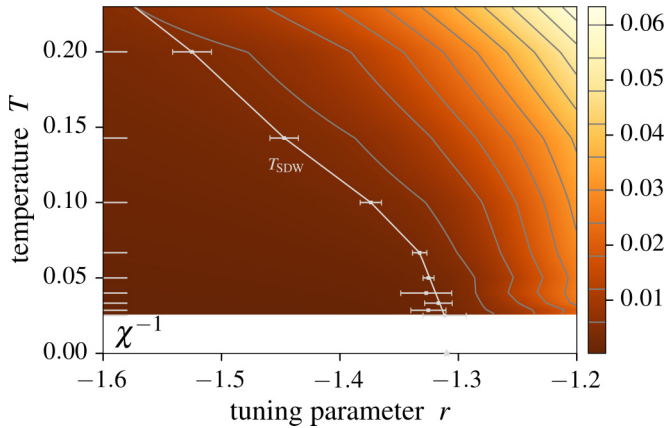


FIG. 3. Inverse SDW susceptibility χ^{-1} across the phase diagram for $\lambda = 1$. We show numerical data obtained at $L = 14$ at the temperatures that are indicated by the ticks on the inside of the plot. Intermediate temperatures are interpolated linearly, while the high resolution in the tuning parameter r is achieved by reweighting. Contour lines of χ^{-1} are marked gray.

Over a broader range of parameters, the maximum SC transition temperature T_c^{\max} grows monotonically with increasing of either the Yukawa coupling or the boson velocity c , as illustrated in Fig. 4. Up to an intermediate coupling strength $\lambda \approx 3$, T_c^{\max} rapidly grows as $T_c^{\max} \propto \lambda^2$, eventually saturating at stronger coupling. Qualitatively, these trends are in agreement with results from Eliashberg theory [43].

III. MAGNETIC CORRELATIONS

We start our discussion of the quantum critical behavior of model (2) with an examination of magnetic fluctuations across its entire finite-temperature phase diagram. We probe the formation of magnetic correlations both through the susceptibility of the bosonic order parameter, $\vec{\varphi}$, and through a fermionic bilinear of the same symmetry, which we evaluate

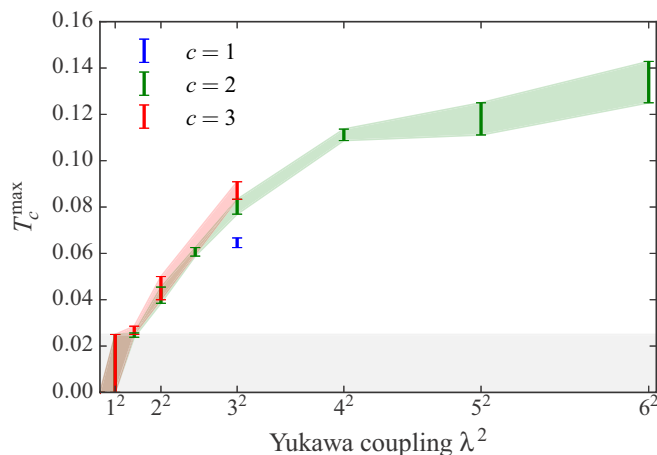


FIG. 4. The maximal superconducting transition temperature T_c^{\max} for different values of the Yukawa coupling λ and (bare) boson velocity c . The hatched gray region indicates temperatures $T < 0.025$, which are beyond our numerically accessible temperature range.

independently in the same numerical simulations of the action (2). As we show below, both susceptibilities exhibit the same behavior, supporting the robustness of our conclusions to be presented.

A. Bosonic SDW susceptibility

We first consider the bosonic susceptibility calculated from the SDW order parameter $\vec{\varphi}$ in action (2)

$$\chi(\mathbf{q}, i\omega_n, r, T) = \sum_i \int_0^\beta d\tau e^{i\omega_n \tau - i\mathbf{q} \cdot \mathbf{r}_i} \langle \vec{\varphi}_i(\tau) \cdot \vec{\varphi}_0(0) \rangle \quad (3)$$

for a given momentum \mathbf{q} and Matsubara frequency $\omega_n = 2\pi nT$. The expectation values are estimated in a DQMC simulation run at finite temperature T and for a specific value of the tuning parameter r , indicated here as explicit parameters. At low temperature, we use the following form to fit the data, inspired by Hertz theory [5]:

$$\begin{aligned} \chi_0^{-1}(\mathbf{q}, i\omega_n, r, T \rightarrow 0) \\ = a_q(\mathbf{q} - \mathbf{Q})^2 + a_\omega |\omega_n| + a_r(r - r_{c0}), \end{aligned} \quad (4)$$

where a_q , a_ω , and a_r are nonuniversal fitting parameters that describe the momentum dependence in the vicinity of the ordering wave vector $\mathbf{Q} = (\pi, \pi)$, Landau damping, and the dependence on the tuning parameter r , respectively. The fitting parameter r_{c0} indicates the location of the divergence of χ_0 . Due to the appearance of a superconducting phase at low temperatures, r_{c0} may differ from the actual location of the QPT at $r = r_c$. However, within our numerical resolution, we find $r_{c0} \approx r_c$, where r_c is obtained by extrapolating the finite-temperature transition line $T_{\text{SDW}} \rightarrow 0$, as shown in the phase diagrams of Fig. 2.

Running extensive DQMC simulations for system sizes $L = 8, 10, \dots, 14$, we have evaluated χ across the three principal phase diagrams of Fig. 2 for different values of the Yukawa coupling $\lambda = 1, 1.5, 2$ and bare bosonic velocity $c = 3$. Restricting our analysis to the magnetically disordered side for each coupling and to temperature scales above the superconducting phase, we find that our calculated susceptibilities are in good agreement with the functional form of Eq. (1). The consistency with Eq. (4) is illustrated in the panels of Fig. 5, which show data collapses for a range of small momenta $\mathbf{q} - \mathbf{Q}$, small Matsubara frequencies, low temperatures $T \leq 0.1$ and tuning parameters $r \geq r_{c0}$. Finite-size effects are rather small. Considering the variation of the Yukawa coupling λ , we find that the fit to the functional form (4) is slightly worse for stronger coupling λ , which is also indicated by the larger spread of the data points. This decreasing fit quality may be a consequence of the smaller temperature window available above the superconducting T_c , as well as the associated regime of superconducting fluctuations at $T \gtrsim T_c$ [28], which increases with Yukawa coupling (see also Fig. 4).

With the data collapse of Fig. 5 asserting the general validity of the functional form (4), we now take a closer look at its individual dependence on tuning parameter, frequency, and momentum. First, the dependence on the tuning parameter r is illustrated for the inverse susceptibility $\chi^{-1}(\mathbf{q} = \mathbf{Q}, i\omega_n = 0)$ in Fig. 6 (for $\lambda = 1.5$ and $T = 0.1$). For tuning parameters $r \gtrsim r_{c0} = 0.6$ we find that the data for different system sizes

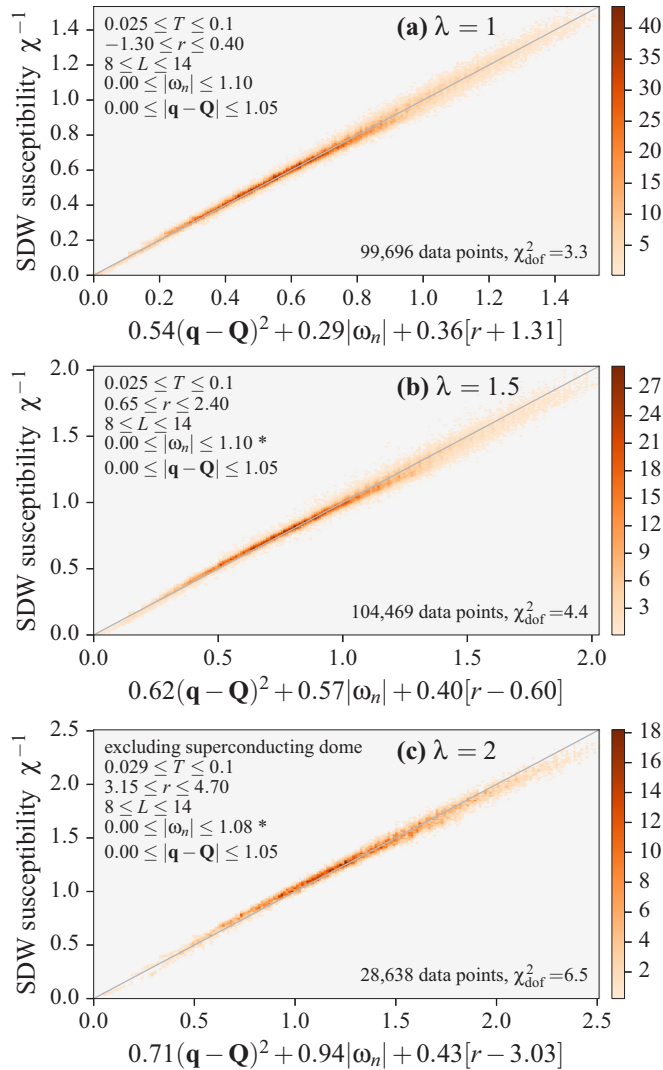


FIG. 5. Comparison between the inverse SDW susceptibility χ^{-1} and the functional form $\chi_0^{-1} = a_q(\mathbf{q} - \mathbf{Q})^2 + a_\omega|\omega_n| + a_r(r - r_{c0})$, which has been fitted for small frequencies ω_n and momenta $\mathbf{q} - \mathbf{Q}$ at low temperatures T and tuning parameters $r > r_{c0}$ in the magnetically disordered phase, for (a) $\lambda = 1$, (b) 1.5, and (c) 2. Data inside the superconducting phase have been excluded from the fit. For temperatures $T \leq 2T_c^{\text{max}}$ we restrict the fit to finite frequencies $|\omega_n| > 0$. The correspondence of χ^{-1} with the fitted form is shown in the form of 2D histograms over all data points, which are normalized over the total area. In each fit we have minimized $\chi_{\text{dof}}^2 = \frac{1}{N_{\text{dof}}} \sum \left[\frac{\chi^{-1} - \chi_0^{-1}}{\varepsilon} \right]^2$, where N_{dof} is the number of degrees of freedom of the fit and ε is the statistical error of the data.

follows a linear dependence. The moderate deviation from a perfect kinklike behavior at r_{c0} is likely a combination of finite-size and finite-temperature effects (see also the finite-size trend shown in the inset of Fig. 6). A very similar picture emerges for the two other coupling parameters $\lambda = 1$ and $\lambda = 2$, for which we show analogous plots in Fig. 19 of Appendix B.

Turning to the frequency dependence of $\chi^{-1}(\mathbf{q}, i\omega_n)$ next, we find that for a range of values $r \geq r_{c0}$ the frequency dependence is linear for small Matsubara frequencies ω_n with an apparent cusp at $\omega_n = 0$, signaling overdamped dynamics

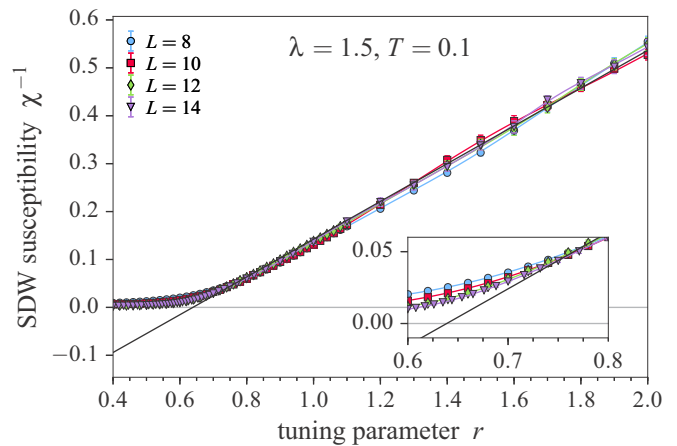


FIG. 6. Bosonic SDW susceptibility $\chi^{-1}(\mathbf{q} = \mathbf{Q}, i\omega_n = 0)$ as a function of the tuning parameter r for $\lambda = 1.5$ at $T = 0.1$. The black line is a linear fit for $r > 0.7$ and $L = 14$. Continuous colored lines through data points have been obtained by a reweighting analysis.

of the order parameter field. This holds both for $\mathbf{q} = \mathbf{Q}$ and for small finite momentum differences $\mathbf{q} - \mathbf{Q}$. See Fig. 7 for an illustration at $\lambda = 1.5$ and Appendix B with Fig. 20 for $\lambda = 1$ and $\lambda = 2$. At finite Matsubara frequencies ω_n , finite-size effects are negligibly small, as evident in the data collapse of χ^{-1} for different system sizes in the left panel in Fig. 7.

To establish the presence of a $|\omega_n|$ term in χ^{-1} , we fit it at low frequencies to the form $b_0 + b_1|\omega_n| + b_2\omega_n^2$. The fits are shown in Fig. 7. The $|\omega_n|$ contribution is clearly dominant in this frequency range. Inside the superconducting phase, the $|\omega_n|$ term is suppressed (see Fig. 24 in Appendix B). This is presumably due to gapping out of the fermions.

Third, for the same range of r , the momentum dependence of $\chi^{-1}(\mathbf{q}, i\omega_n)$ is consistent with a quadratic form in $\mathbf{q} - \mathbf{Q}$, which holds both for $\omega_n = 0$ and small finite frequencies ω_n .

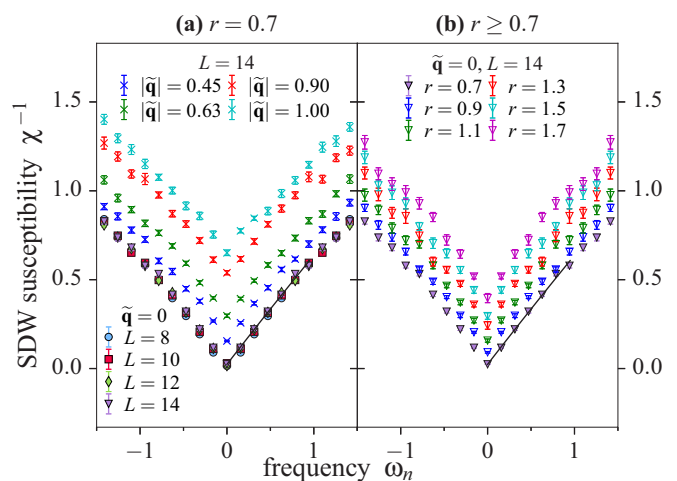


FIG. 7. Frequency dependence of the inverse bosonic SDW susceptibility χ^{-1} for $\lambda = 1.5$ at $T = 1/40$ (a) shown at $r \approx r_{c0}$ for various momenta $\mathbf{q} = \mathbf{Q} + \tilde{\mathbf{q}}$ and (b) shown at various values $r > r_{c0}$ for $\mathbf{q} = \mathbf{Q}$. The black line is the best fit of a second degree polynomial $b_0 + b_1|\omega_n| + b_2\omega_n^2$ to the $\mathbf{q} = \mathbf{Q}$, $L = 14$ low-frequency data, yielding a basically straight line.

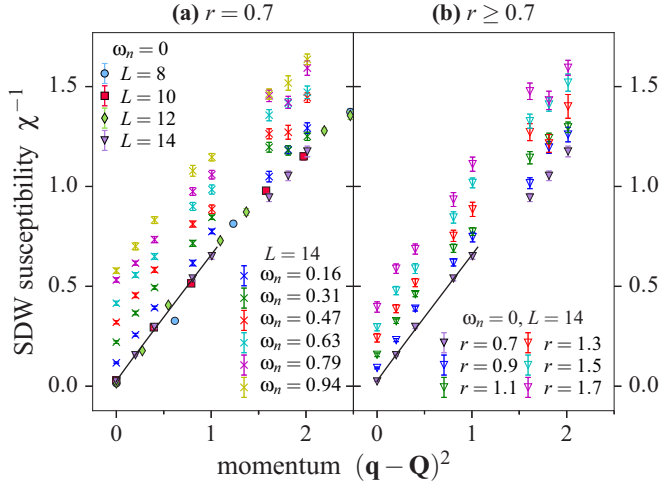


FIG. 8. Inverse bosonic SDW susceptibility χ^{-1} as a function of momentum $\mathbf{q} = \mathbf{Q} + \tilde{\mathbf{q}}$ for $\lambda = 1.5$ at $T = 1/40$ (a) shown at $r \approx r_{c0}$ for various frequencies ω_n and (b) shown at various values $r \gtrsim r_{c0}$ for $\omega_n = 0$. The black line is the best fit of $a_0 + a_2 \tilde{\mathbf{q}}^2$ to the $\omega_n = 0$, $L = 14$ small-momentum data.

(See Fig. 8 for $\lambda = 1.5$ and Appendix B with Fig. 21 for $\lambda = 1$ and $\lambda = 2$.) Note that due to the discretization of the Brillouin zone, finite-size effects are more pronounced here than for the frequency dependence.

B. Fermion bilinear SDW susceptibility

An important independent confirmation that the form (4) is generic to the quantum critical regime is to affirm that it also holds for other SDW order parameters that have the same symmetry. We have examined the correlations of a *fermion* bilinear order parameter:

$$S_{xx}(\mathbf{q}, i\omega_n, r, T) = \sum_i \int_0^\beta d\tau e^{i\omega_n \tau - i\mathbf{q} \cdot \mathbf{r}_i} \langle S_i^x(\tau) S_0^x(0) \rangle. \quad (5)$$

In the estimation of S_{xx} , we make use of spin rotational symmetry around the z axis, $\langle S_i^x(\tau) S_0^x(0) \rangle = \langle S_i^y(\tau) S_0^y(0) \rangle$. Here, S_i^x and S_i^y are interflavor fermion spin operators, which are given by

$$\vec{S}_i = (S_i^x, S_i^y, S_i^z) = \sum_{s,s'} \vec{s}_{ss'} \psi_{xis}^\dagger \psi_{yis'} + \text{H.c.} \quad (6)$$

Indeed, we find that at small frequencies and momenta, the fermion bilinear SDW susceptibility S_{xx} follows the same functional form (4) as the bosonic SDW susceptibility χ discussed above. The momenta and frequency dependencies of the fermionic bilinear susceptibility at $\lambda = 1.5$ are shown in Fig. 9, with the respective dependencies of the bosonic susceptibility appearing in Figs. 7 and 8. Additional data for the fermionic SDW susceptibility at $\lambda = 1$ and $\lambda = 2$ is given in Fig. 22 of Appendix B. In summary, the dependence of both the bosonic and fermionic SDW susceptibilities on the tuning parameter, frequency, and momentum stand in good agreement with the form (4).

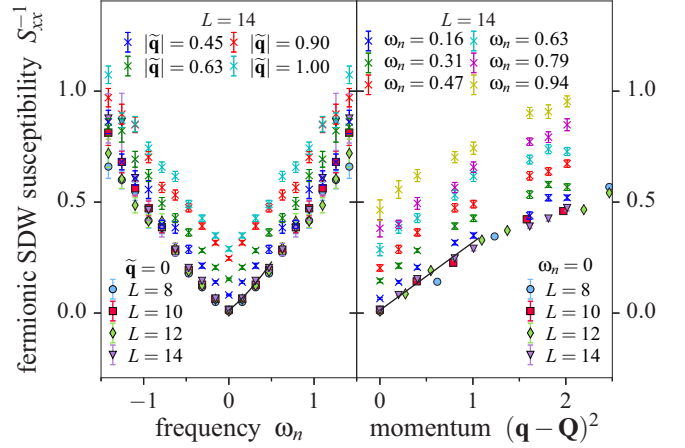


FIG. 9. Inverse fermionic SDW susceptibility S_{xx}^{-1} for $\lambda = 1.5$ at $T = 1/40$ and $r = 0.7 \approx r_{c0}$. (Left-hand side) Frequency dependence for various momenta $\mathbf{q} = \mathbf{Q} + \tilde{\mathbf{q}}$. The black line is a fit of the second degree polynomial $b_0 + b_1 |\omega_n| + b_2 \omega_n^2$ to the $\mathbf{q} = \mathbf{Q}$, $L = 14$ low-frequency data, yielding a basically straight line. (Right-hand side) Momentum dependence for various frequencies ω_n . The black line is a fit of $a_0 + a_2 \tilde{\mathbf{q}}^2$ to the $\omega_n = 0$, $L = 14$ small-momentum data.

C. Temperature dependence

We now turn to the temperature dependence of the numerically computed bosonic and fermionic SDW susceptibilities χ^{-1} and S_{xx}^{-1} . Our numerical data for the temperature dependence of χ^{-1} and S_{xx}^{-1} are shown in Fig. 10 for fixed Yukawa coupling $\lambda = 1.5$ and two different values of the tuning parameter on the paramagnetic side of the QCP, i.e., for $r > r_{c0}$. These data are complemented with similar results for $\lambda = 1$ and 2 in Fig. 23 of Appendix B.

Evidently, the data show different scaling regimes with increasing temperature. At sufficiently high temperatures, $T \gtrsim 0.35$, the susceptibilities $\chi^{-1}(\mathbf{q} = \mathbf{Q}, i\omega_n = 0)$ and $S_{xx}^{-1}(\mathbf{q} = \mathbf{Q}, i\omega_n = 0)$ are approximately linearly dependent on temperature, as shown in the insets of Fig. 10. In an intermediate temperature regime, however, we observe a crossover to a different functional temperature dependence as shown in the main panels of Fig. 10. In this intermediate temperature window $0.05 \lesssim T \lesssim 0.35$, our numerical data are found to reasonably fit functions of the *quadratic* form $a_0 + a_2 T^\alpha$ with $\alpha \simeq 2 \pm 0.3$. Unlike the leading dependencies on the tuning parameter, frequency and momentum discussed in the previous section, this power-law dependence is not as robust. Note that the crossover temperature between the high- T linear and intermediate- T quadratic behaviors does not depend strongly on the tuning parameter r . Notably, even for $r \approx r_{c0}$, this intermediate regime does not disappear.

At still lower temperatures $T \lesssim 0.05$, our data might indicate a second crossover to yet different behavior. With the tuning parameter r tuned close to its critical value r_{c0} both χ and S_{xx} are found to be nonmonotonic for the smallest temperatures and largest system sizes accessed in this study. The apparent upturn, whose precise location is hard to determine due to finite-size effects (which are strongest for $r \approx r_{c0}$) and the enhanced statistical uncertainty at low temperatures, is most likely a precursor effect of superconductivity [28], which

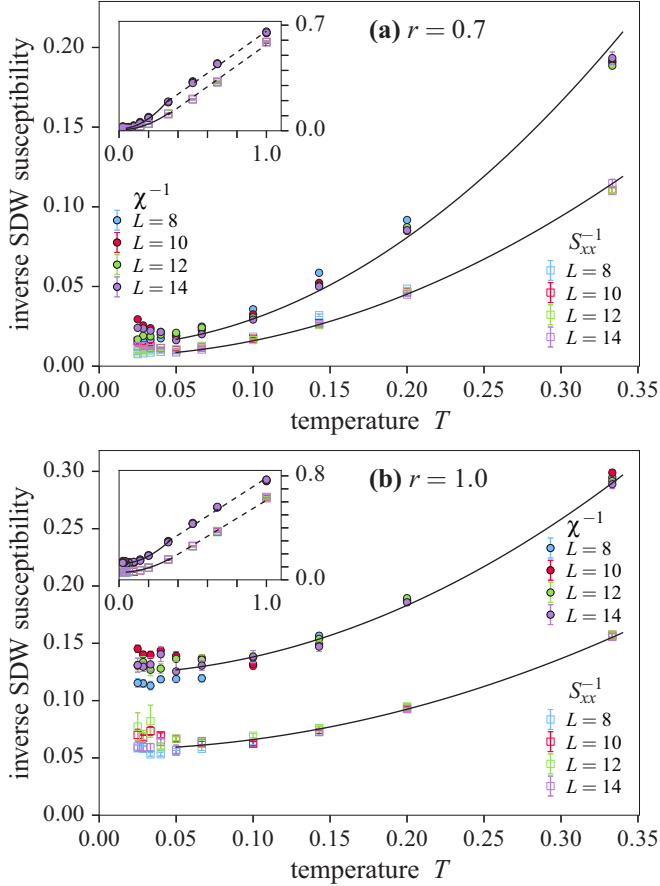


FIG. 10. Inverse bosonic SDW susceptibility $\chi^{-1}(\mathbf{q} = \mathbf{Q}, i\omega_n = 0)$ and inverse fermionic SDW susceptibility $S_{xx}^{-1}(\mathbf{q} = \mathbf{Q}, i\omega_n = 0)$ as a function of temperature for $\lambda = 1.5$ at (a) $r = 0.7 \approx r_{c0}$ and at (b) $r = 1.0 > r_{c0}$. Solid lines indicate fits of $a_0 + a_2 T^2$ to the $L = 14$ data at intermediate temperatures. Dashed lines are linear fits to the high-temperature data. In each figure the inset shows the same data as the main plot over a more extended temperature range.

for $\lambda = 1.5$ sets in just at the lowest temperature we have accessed in this work, $T_c \approx 1/40$. For larger Yukawa coupling $\lambda = 2$, where T_c is higher, this nonmonotonic behavior is indeed found to be more pronounced as shown in Fig. 23 of Appendix B.

Note that over the range of temperatures displayed in Fig. 3 the leading temperature dependence of χ^{-1} is quadratic. This is reflected in the contour lines of χ^{-1} in the r - T plane, which have a form $T \sim \sqrt{\chi^{-1} - a_r(r - r_{c0})}$, approaching infinite slope at low temperatures.

Since the data do not allow us to identify a simple functional form for the temperature dependence of χ^{-1} , we have opted against taking into account any temperature dependence in the fits for the data collapses shown in Fig. 5. Instead we have constrained the included data to $T < 0.1$ where the overall temperature dependence is rather weak.

IV. SINGLE-FERMION CORRELATIONS

We now turn to examine the fermionic spectral properties in the metallic state above the superconducting T_c . As our DQMC simulations are performed in imaginary time, there

is an inherent difficulty in probing real-time dynamics. To partially circumvent this issue, we use the relation [44]

$$G_{\mathbf{k}}(\tau) = \int_{-\infty}^{\infty} d\omega \frac{e^{-\omega(\tau - \beta/2)}}{2 \cosh \beta\omega/2} A_{\mathbf{k}}(\omega), \quad (7)$$

which connects the readily available imaginary-time ordered Green's function $G_{\mathbf{k}}(\tau) = \langle \psi_{\mathbf{k}}(\tau) \psi_{\mathbf{k}}^{\dagger}(0) \rangle$, where $0 \leq \tau \leq \beta$, with the spectral function $A_{\mathbf{k}}(\omega)$ of interest. Here and in the following, we focus on a single flavor of fermions ψ_y , suppressing band and spin indices. Close inspection of (7) reveals that the behavior of the Green's function $G_{\mathbf{k}}(\tau)$ at long times, i.e., for imaginary times close to $\tau = \beta/2$, provides information about the spectral function integrated over a frequency window of width T .

In Fig. 11, we present the evolution of the Fermi surface across the phase diagram. For orientation, the Fermi surfaces of the noninteracting system are shown in panel (a). In panels (b)–(d) we show $G_{\mathbf{k}}(\tau = \beta/2)$ across a quadrant of the Brillouin zone for a low temperature $T = 0.05 \approx 2T_c^{\max}$. Near the magnetic QCP (panel c), there is a clear loss of spectral weight in the immediate vicinity of the hot spots, as compared to the magnetically disordered phase (panel d). Upon entering the magnetic phase (panel b), a gap opens around the hot spots. In this section we focus on the parameter set $\lambda = 1.5$ and $c = 3$. The DQMC simulations are carried out with different sets of twisted boundary conditions (see Appendix A for details), providing a four-fold enhancement in \mathbf{k} -space resolution.

A Fermi liquid is usually characterized by the quasiparticle weight $Z_{\mathbf{k}_F}$ and the Fermi velocity $\mathbf{v}_{\mathbf{k}_F}$. We note that these quantities are only strictly defined at zero temperature. Given that the zero-temperature ground state of our model is probably always superconducting, our strategy is to consider finite-temperature proxies for $Z_{\mathbf{k}_F}$ and $\mathbf{v}_{\mathbf{k}_F}$, and study their behavior over an intermediate temperature range $E_F > T > T_c$. Such proxies, $Z_{\mathbf{k}_F}^{\tau}(T)$ and $\mathbf{v}_{\mathbf{k}_F}^{\tau}(T)$, can be extracted by considering the imaginary time dependence of $G_{\mathbf{k}}(\tau)$ near $\tau = \beta/2$ and fitting it to the Fermi liquid form [41]

$$G_{\mathbf{k}}(\tau \sim \beta/2) = Z_{\mathbf{k}}^{\tau}(T) \frac{e^{-\epsilon_{\mathbf{k}}(\tau - \beta/2)}}{2 \cosh(\frac{\beta\epsilon_{\mathbf{k}}}{2})}, \quad (8)$$

where $\epsilon_{\mathbf{k}} = \mathbf{v}_{\mathbf{k}_F}^{\tau}(T) \cdot (\mathbf{k} - \mathbf{k}_F)$.

In a complementary approach we consider the Matsubara frequency dependence of the Green's function $G_{\mathbf{k}}(\omega_n) = \int_0^{\beta} d\tau e^{i\omega_n\tau} G_{\mathbf{k}}(\tau)$. In a Fermi liquid at low temperatures, we have [45]

$$G_{\mathbf{k}}(\omega_n) \approx Z_{\mathbf{k}}[i\omega_n - \mathbf{v}_{\mathbf{k}_F} \cdot (\mathbf{k} - \mathbf{k}_F)]^{-1} \quad (9)$$

up to higher-order terms in temperature, frequency, or the distance from the Fermi surface. It is then natural to define the finite-temperature quantities

$$Z_{\mathbf{k}_F}^{\omega}(T) = \frac{\omega_1}{\text{Im } G_{\mathbf{k}_F}^{-1}(\omega_1)} \quad (10)$$

and

$$\mathbf{v}_{\mathbf{k}_F}^{\omega}(T) = \omega_1 \left. \frac{\partial \text{Re } G_{\mathbf{k}}(\omega_1)}{\partial \mathbf{k} \text{ Im } G_{\mathbf{k}}(\omega_1)} \right|_{\mathbf{k}=\mathbf{k}_F}, \quad (11)$$

where $\omega_1 = \pi T$ is the first Matsubara frequency at temperature T . In the zero-temperature limit, $Z_{\mathbf{k}_F}^{\omega}(T \rightarrow 0) =$

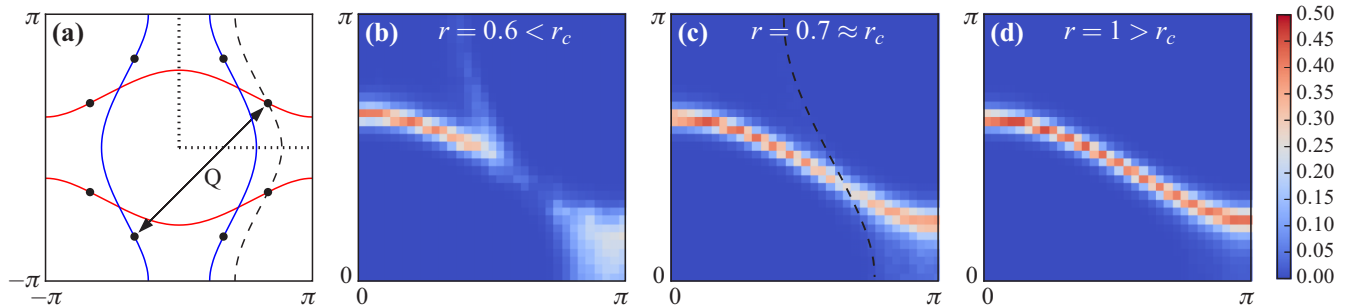


FIG. 11. (a) Noninteracting Fermi surfaces. A pair of hot spots is connected by the magnetic ordering wave vector \mathbf{Q} . The dashed curve corresponds to the Fermi surface of the ψ_x band, shifted by \mathbf{Q} , with a hot spot now at the intersection with the ψ_y band. (b)–(d) Color-coded Green’s function $G_{\mathbf{k}}(\tau = \beta/2)$ evaluated for the ψ_y fermions on a quadrant of the Brillouin zone, dotted in (a), for three values of the tuning parameter r . The dashed curve in panel (c) corresponds to the shifted noninteracting ψ_x Fermi surface. The parameters used here are $L = 16$, $T = 0.05$, $\lambda = 1.5$, and $c = 3$. Results of simulations with different boundary conditions are combined for enhanced momentum resolution.

$Z_{\mathbf{k}_F}^{\tau}(T \rightarrow 0) = Z_{\mathbf{k}_F}$, and similarly for $\mathbf{v}_{\mathbf{k}_F}$. We therefore use the finite-temperature observables (10) and (11) as alternative proxies for the quasiparticle spectral weight and Fermi velocity, respectively.

Figure 12 shows the momentum dependence of $Z_{\mathbf{k}}^{\tau}$ for temperature $T = 1/20$. With r tuned close to the location of the QCP at r_c , $Z_{\mathbf{k}}^{\tau}$ is suppressed in the vicinity of the hot spots, as shown for one quadrant of the Brillouin zone in Fig. 12(a) and along the Fermi surface in Fig. 12(c). This stands in sharp

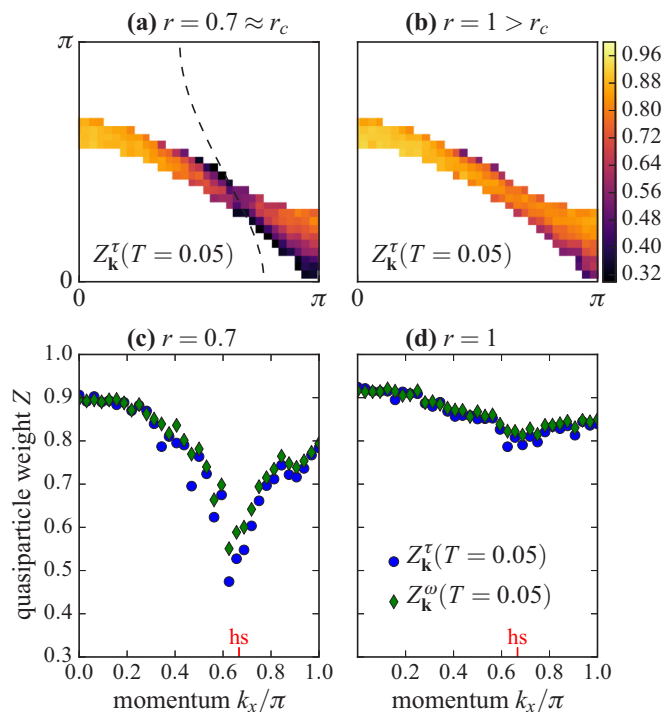


FIG. 12. (a) and (b) The quasiparticle weight $Z_{\mathbf{k}}^{\tau}(T = 0.05)$ in a quadrant of the Brillouin zone. The dashed line in panel (a) corresponds to the noninteracting Fermi surface of the ψ_x fermions, shifted by \mathbf{Q} . (c) and (d) The quasiparticle weights $Z_{\mathbf{k}}^{\tau}(T = 0.05)$ and $Z_{\mathbf{k}}^{\omega}(T = 0.05)$ along the Fermi surface. The location of the hot spot is indicated by the red marker. Here, we show data obtained for $L = 16$.

contrast to the featureless behavior of $Z_{\mathbf{k}}^{\tau}$ in the magnetically disordered phase, as shown in Figs. 12(b) and 12(d). We find qualitative agreement between the two proxies $Z_{\mathbf{k}}^{\tau}$ and $Z_{\mathbf{k}}^{\omega}$ throughout, as illustrated in panels (c) and (d) of Fig. 12. Here, we numerically identify and track the Fermi surface as the maxima of $G_{\mathbf{k}}(\tau = \beta/2)$ at fixed k_x .

The temperature dependence of $Z_{\mathbf{k}}^{\tau}(T)$ is shown in Fig. 13. For momenta away from the hot spots, we find $Z_{\mathbf{k}}^{\tau}(T)$ to be nearly flat in temperature and to approach a constant as $T \rightarrow 0$. A different picture emerges at the hot spots, i.e., for $\mathbf{k} = \mathbf{k}_{hs}$. Here, $Z_{\mathbf{k}=\mathbf{k}_{hs}}^{\tau}(T)$ remains flat only in the magnetically disordered phase $r > r_c$, whereas the quasiparticle weight $Z_{\mathbf{k}=\mathbf{k}_{hs}}^{\tau}(T)$ decreases substantially at the critical coupling $r_c \approx 0.7$ as the temperature is lowered towards the QCP, see Fig. 13(a). While our numerical data do not allow for a simple extrapolation towards $T = 0$, the results are not inconsistent with a vanishing of $Z_{\mathbf{k}=\mathbf{k}_{hs}}$, indicating a breakdown of Fermi-liquid behavior at this point.

Figure 14 shows the velocity $v_{\mathbf{k}_F}(T = 0.05)$ along the Fermi surface. The qualitative behavior of the velocity does not differ substantially between $r = 0.7 \approx r_c$ [Fig. 14(a)] and $r = 1 > r_c$ [Fig. 14(b)]. The insets show the ratio

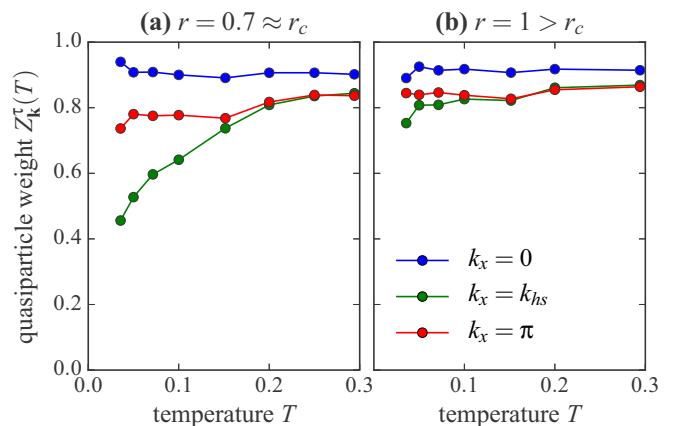


FIG. 13. Temperature dependence of the quasiparticle weight $Z_{\mathbf{k}}^{\tau}(T)$ for different momenta k_x along the Fermi surface (a) in the vicinity of the QCP at r_c and (b) in the disordered side. Here we show data obtained for $L = 16$.

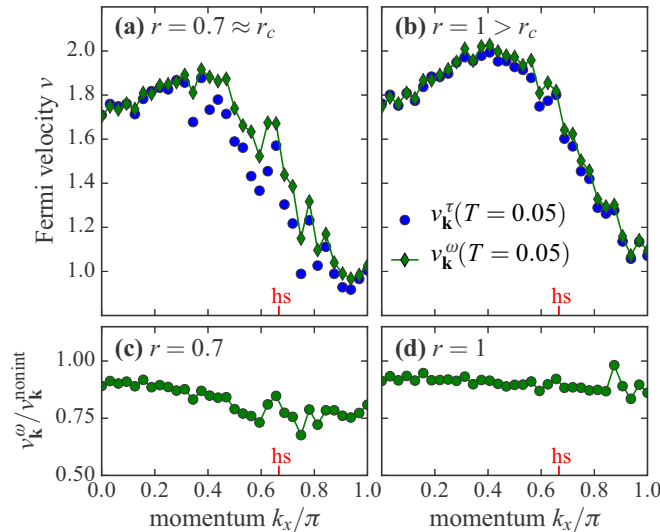


FIG. 14. (a) and (b) The finite-temperature proxies to the velocity $v_{\mathbf{k}}$ along the Fermi surface. (c)-(d) The velocity renormalization $v_{\mathbf{k}}^{\omega}(T = 0.05)/v_{\mathbf{k}}^{\text{nonint}}$. The location of the hot spot is indicated by the red marker. Here we show data obtained for $L = 16$ at $T = 0.05$.

$v_{\mathbf{k}_F}(T = 0.05)/v_{\mathbf{k}}^{\text{nonint}}$, where $v_{\mathbf{k}}^{\text{nonint}}$ is the Fermi velocity of the noninteracting system. A small feature might be visible in the vicinity of the hot spot, but there is certainly no evidence of a substantial suppression of $v_{\mathbf{k}_{hs}}$ close to r_c .

Having found a substantial suppression of the quasiparticle weight tuned close to the QCP, we now directly examine the frequency dependence of the self-energy, $\Sigma_{\mathbf{k}}(\omega_n)$, defined via $G_{\mathbf{k}}(\omega_n) = (i\omega_n - \epsilon_{\mathbf{k}} - \Sigma_{\mathbf{k}}(\omega_n))^{-1}$. The imaginary part of the self-energy is shown in Fig. 15. With $r = 0.7 \approx r_c$ tuned close to the QCP, see Fig. 15(a), the self-energy close to the hot spots is found to be nearly frequency independent, consistent with a *constant*, yet small, scattering rate $\gamma = -\text{Im} \Sigma_{\mathbf{k}_{hs}}(\omega_n \rightarrow 0^+) \approx 0.13$, which is only weakly dependent on temperature.

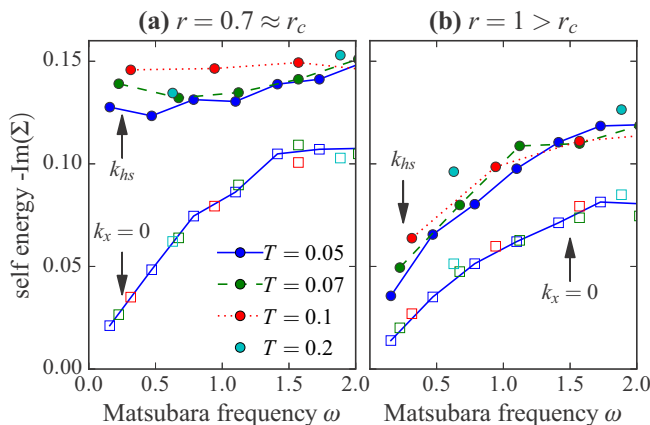


FIG. 15. The imaginary part of the Matsubara self-energy $\text{Im} \Sigma$ for different temperatures and two momenta along the Fermi surface, (a) in the vicinity of the QCP at r_c and (b) on the disordered side. Here we show data obtained for $L = 14$. The data for $\mathbf{k} = \mathbf{k}_{hs}$ are indicated by full circles, the momentum away from the hot spot is indicated by empty squares.

Away from the hot spot the self-energy is linear with frequency, with a substantially smaller intercept. Moving away from the critical point [Fig. 15(b)], the self-energy at all momenta decreases rapidly as the frequency is lowered.

V. SUPERCONDUCTING STATE

After concentrating our discussion on the manifestation of quantum critical behavior in the normal state, we now consider the effect of the QCP on the superconducting state that emerges in its vicinity. We begin by considering the fermionic Green's function for temperatures $T \ll T_c$. In this regime, the single-particle excitation energy $E_{\mathbf{k}}$ can be extracted, as demonstrated in Appendix D, from the decay of the single-particle Green's function at intermediate times $\tau_0 < \tau < \beta/2$ (where τ_0 is a microscopic scale). The so-extracted excitation energy $E_{\mathbf{k}}$ is plotted in Fig. 16, which shows that, across the Brillouin zone, $E_{\mathbf{k}}$ has a broad minimum in the vicinity of the noninteracting Fermi surface. From these momentum-resolved energy bands, we extract the superconducting gap Δ_{k_x} as the minimum of $E_{\mathbf{k}}$ with respect to k_y . As seen in Fig. 16(b), the superconducting gap Δ_{k_x} varies smoothly across momentum space, without any significant features at the hot spots. In this section we choose parameters $\lambda = 3$ and $c = 2$, as in Ref. [28]. The maximal T_c for this value of λ is high enough to allow us to explore properties of the superconducting state significantly below T_c .

At higher temperatures, close to T_c , additional information can be obtained by considering the momentum-resolved superconducting susceptibility

$$P_{\mathbf{k}\alpha;\mathbf{k}'\alpha'} = \int_0^{\beta} d\tau \langle \Psi_{\mathbf{k}\alpha}(\tau) \Psi_{\mathbf{k}'\alpha'}^{\dagger}(0) \rangle, \quad (12)$$

where $\Psi_{\mathbf{k}\alpha} = \frac{1}{2}(\psi_{\mathbf{k}\alpha\uparrow}\psi_{-\mathbf{k}\alpha\downarrow} - \psi_{\mathbf{k}\alpha\downarrow}\psi_{-\mathbf{k}\alpha\uparrow})$ is the singlet superconducting pair amplitude on the band $\alpha = x, y$. Here we focus on the intraband, spin-singlet channel since it is the leading instability [17,28]. Figure 17 shows the optimal pair amplitude $\Psi_{\mathbf{k}\alpha}^{\text{opt}}$, corresponding to the maximal eigenvalue of the matrix $P_{\mathbf{k}\alpha;\mathbf{k}'\alpha'}$ at a temperature slightly above T_c . The pair amplitude of the band $\alpha = y$, shown in Fig. 17(a), is of the opposite sign to the amplitude on the band $\alpha = x$, shown in

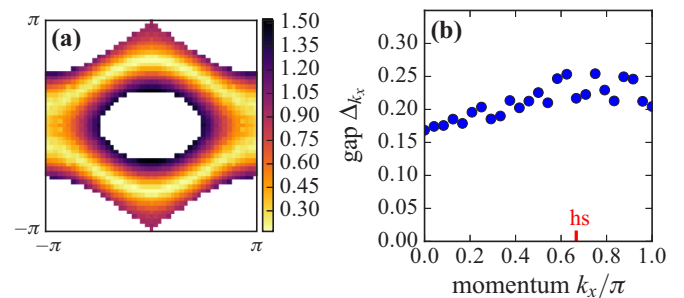


FIG. 16. (a) Single-particle excitation energy $E_{\mathbf{k}}$ of the ψ_y fermions, as extracted from the imaginary-time evolution of the Green's function $G_{\mathbf{k}}(\tau)$ across the Brillouin zone, cf. Fig. 26 of the appendix. (b) Single-particle gap Δ_{k_x} . For both panels, data are for parameters $\lambda = 3$, $c = 2$, $r = 10.2$ and $T = 0.025 \approx 0.3T_c$ [28] and a system size of $L = 12$. Several twisted boundary conditions were combined for a fourfold enhancement of the resolution in \mathbf{k} space, see Appendix A.

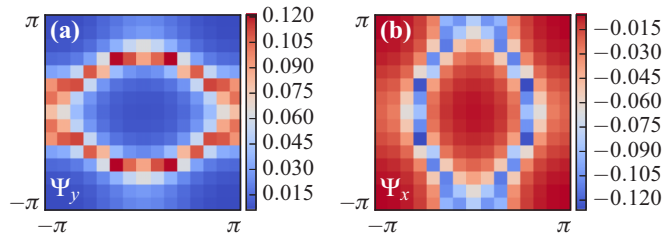


FIG. 17. Optimal pair amplitude $\Psi_{\mathbf{k}\alpha}^{\text{opt}}$ with the band $\alpha = y$ shown in (a) and the band $\alpha = x$ shown in (b). Data are calculated for parameters $\lambda = 3$, $c = 2$, $r = 10.2$, and $T = 0.1 \approx 1.2T_c$ and system size $L = 14$.

Fig. 17(b). In fact, the two amplitudes are related precisely by a $\pi/2$ rotation, highlighting the d -wave symmetry of the superconducting order parameter. The optimal pair amplitude is found to be maximal around the (noninteracting) Fermi surface. The variation of $\Psi_{\mathbf{k}\alpha}^{\text{opt}}$ along the Fermi surface is weak, again showing no strong features at the hot spots.

VI. DISCUSSION

In this work, we have explored the properties of a metal on the verge of an SDW transition. We focused on the critical regime upon approaching the transition, characterized by a rapid growth of the SDW correlations, but still above the superconducting transition temperature. Our main conclusion is that, in this regime, the SDW correlations are remarkably well described by a form similar to that predicted by Hertz-Millis theory, Eq. (1) (although the temperature dependence of the SDW susceptibility deviates from the expected form). This holds both for the correlations of the bosonic SDW order parameter field, and for an SDW order parameter defined in terms of a fermion bilinear. In the same regime, we find evidence for strong scattering of quasiparticles near the hotspots, leading to a breakdown of Fermi liquid theory at these points on the Fermi surface. The scattering rate at the hotspots (extracted from the fermion self-energy) is only weakly temperature and frequency dependent, down to $T \approx 2T_c$, where we suspect that superconducting fluctuations begin to play a role; it is out of this unusual metallic state that the superconducting phase emerges.

In addition, we have studied the structure of the superconducting gap near the SDW transition. Unlike the single-fermion Green’s function in the normal state, it does not have a sharp feature at the hot spots; rather, it is found to vary smoothly across the Fermi surface. Experimentally, a broad maximum of the superconducting gap near the hot spots was observed in a certain electron doped cuprate [46]. Eliashberg theory predicts a peak of the gap function at the hot spots at weak coupling [47] and it remains to be seen whether such behavior appears in our model at weaker coupling.

It is interesting to discuss our results in the context of the existing theories of metallic SDW transitions. First, the fact that Hertz-Millis theory successfully describes many features of our data is nontrivial, in view of the fact that it has no formal justification, even in the large N limit [12,14]. However, as we saw, an extension of the Hertz-Millis analysis

to finite temperature predicts that at criticality, $\chi(T) \sim 1/T$, in apparent disagreement with our data. This may be due to the limited temperature window we can access without hitting the superconducting T_c , or to effects beyond the one-loop approximation.

An important conclusion of our study is that the SDW critical point is always masked by a superconducting phase.² As a result, it seems likely that the critical metallic regime is never parametrically broad, and one cannot sharply define scaling exponents within the metallic phase.³ As mentioned above, the SDW correlations follow a Hertz-Millis form—and hence it is tempting to associate with them critical exponents, i.e., a mean-field value $\nu = 1/2$ for the correlation length exponent, and a dynamical critical exponent $z = 2$. The fermionic quasiparticles at the hot spots, however, do not exhibit this scaling behavior. In particular, the expected scaling law $\Sigma(\omega_n) \sim \sqrt{\omega_n}$ for the fermion self-energy at the hot spots is not seen within our accessible temperature range.

One can imagine trying to access the “bare” metallic quantum critical point by suppressing the superconducting transition. Presumably, this can be done by adding to the model a term that breaks time-reversal and inversion symmetries (such a term would lift the degeneracy of fermionic states with opposite momenta, and hence remove the Cooper instability). Breaking time-reversal symmetry, however, gives rise to a sign problem, so it is not clear whether the critical behavior can be accessed within the QMC technique.

Alternatively, one could try to understand the metallic regime above T_c in our model as a crossover regime of an underlying “nearby” metallic critical point, where some correlators already exhibit their asymptotic behavior (such as the SDW order parameter correlations), while others do not (e.g., the single-fermion Green’s function). Interestingly, a simple, non-self-consistent one-loop calculation of the fermionic self-energy in our model does show a broad range of temperature and frequency where the self-energy at the hot spot is nearly constant, before eventually settling into the expected $\sqrt{\omega_n}$ behavior (see Appendix C). This calls for a more detailed comparison between our numerically exact DQMC results and a detailed self-consistent one-loop analysis. Preliminary results show that this approximation is surprisingly successful in capturing at least some of the physics of our model [43].

To what extent such a crossover behavior, characterized by a nearly-constant fermionic lifetime at the hotspots, is ubiquitous across different models, as well as in real materials, remains to be seen. It is interesting to note, however, that a similar behavior has been observed in a study of a *nematic* transition in a metal [48]. It would be interesting to systematically look for such behavior in angle-resolved photoemission spectroscopy in the electron-doped cuprates, where anomalously large broadening of the quasiparticle peaks is seen near the hot spots [49].

²Even for the smallest value of λ that we have studied, where the maximal T_c is smaller than the lowest temperature in our study, we see enhancement of diamagnetic fluctuations, indicating that we are not too far above T_c .

³In the superconducting phase, we expect criticality of the $d = 2 + 1$ XY universality class, since the Fermi surface is gapped.

Another important aspect of the metallic state in the critical regime, which we have not addressed in this work, is the electrical conductivity. The optical conductivity may be strongly affected by the presence of an SDW critical point, even without quenched disorder [16,50]. Extracting the conductivity from quantum Monte Carlo simulations requires an analytic continuation, and is therefore intrinsically more difficult (and involves more uncertainties) than calculating thermodynamic and imaginary-time quantities. Nevertheless, we have obtained preliminary results showing strong effects of the critical fluctuations on the low-frequency optical conductivity [51]. A full analysis of the conductivity is deferred to future work.

ACKNOWLEDGMENTS

We thank A. Chubukov and C. Varma for useful discussions on this work and S.-S. Lee for his comments on the manuscript. E. B. and Y. S. also thank R. Fernandes, S.A. Kivelson, S. Lederer, and X. Wang for numerous discussions and collaborations on related topics. E.B. thanks the hospitality of the Aspen Center for Physics, where part of this work was done. The numerical simulations were performed on the CHEOPS cluster at RRZK Cologne, the JUROPA/JURECA clusters at the Forschungszentrum Jülich, and the ATLAS cluster at the Weizmann Institute. Y.S. and E.B. were supported by the Israel Science Foundation under Grant No. 1291/12, by the US-Israel BSF under Grant No. 2014209, and by a Marie Curie reintegration grant. E. B. was supported by an Alon fellowship. M. G. thanks the Bonn-Cologne Graduate School of Physics and Astronomy (BCGS) for support.

M.H.G. and Y.S. have contributed equally to this work.

APPENDIX A: DQMC SIMULATIONS

In this appendix, we elaborate on a number of specific technical aspects of our numerical implementation of the determinantal quantum Monte Carlo (DQMC) approach. We refer readers looking for a more comprehensive discussion of the general DQMC setup to our previous paper [28] and in particular its supplementary online material.

We study the lattice model described by the action (2) at finite temperature in the grand canonical ensemble. After discretizing imaginary time and integrating out the fermionic degrees of freedom, the partition function reads

$$Z = \int D\vec{\varphi} e^{-\Delta\tau \sum_{\tau} L_{\varphi}(\tau)} \det G_{\varphi}^{-1}, \tag{A1}$$

where G_{φ} is the equal-time Green's function matrix for a fixed configuration of the bosonic order parameter field $\vec{\varphi}$. We use an imaginary time step of $\Delta\tau = 0.1$ in all calculations. The DQMC method samples configurations of $\vec{\varphi}$ according to their weight $\exp(-\Delta\tau \sum_{\tau} L_{\varphi}(\tau)) \cdot \det G_{\varphi}^{-1}$. For efficient Monte Carlo sampling, is it highly advantageous to consider models in which the determinant in (A1) is guaranteed to be positive, thereby avoiding the notorious fermion sign problem. For the two-band model that has been proposed in Ref. [17] this is ensured by an antiunitary symmetry of the action [52–54], written in first quantization as

$$\mathcal{U} = is_y \tau_z K \quad \text{with} \quad \mathcal{U}^2 = -\mathbb{1}. \tag{A2}$$

Here, K is the complex conjugation operator and s_y (τ_z) are Pauli matrices acting in spin (flavor) space, respectively.

In this manuscript we have modified the model of Ref. [17] in two regards. First, as in our previous paper [28], we consider an easy-plane SDW order parameter, rather than an $O(3)$ symmetric order parameter used in [17]. Second, we couple the system to a fictitious, spin and band dependent orbital “magnetic” field, whose flux through the system is given by $\vec{\Phi}_{\alpha,s} = \Phi_{\alpha,s}^{(x)} \vec{e}^x + \Phi_{\alpha,s}^{(y)} \vec{e}^y + \Phi_{\alpha,s}^{(z)} \vec{e}^z$. Here, we place the two-dimensional lattice (x, y directions) on a torus. The x and y components of the flux twist the boundary conditions along the y and x directions, respectively, while the z component acts as an orbital magnetic field with a uniform flux per plaquette through the torus. As in the definition of the action (2), $\alpha = x, y$ is a fermion flavor index and $s = \uparrow, \downarrow$ is a spin index. The flux Φ^z is restricted to be an integer multiple of the flux quantum Φ_0 .

In order to preserve the symmetry (A2), fermions of different spin and flavor are coupled to this fictitious flux as

$$\begin{aligned} \vec{\Phi}_{\alpha,\uparrow} &= -\vec{\Phi}_{\alpha,\downarrow} \quad \text{and} \\ \vec{\Phi}_{x,s} &= -\vec{\Phi}_{y,s}, \end{aligned} \tag{A3}$$

with $\vec{\Phi}_{x,\uparrow} = \vec{\Phi}$. Note that the interband sign change is not strictly necessary to avoid the fermion sign problem. Importantly, in the thermodynamic limit $L \rightarrow \infty$ the fictitious field vanishes. In our previous paper [28] and for some of the results in the present one, we have chosen $\vec{\Phi} = (0,0,\Phi_0)$. Although such a flux is useful in reducing spurious finite-size effects at low temperatures [40,41], it also breaks lattice translational symmetry, hampering the analysis of nonlocal, fermionic correlation functions such as the momentum-resolved Green's function. In order to measure such quantities, for the present paper, we have run additional simulations without applying a perpendicular flux $\Phi^{(z)}$, but instead with *in-plane* fields, such that $\vec{\Phi} = (n_x, n_y, 0) \frac{\Phi_0}{4}$, where $n_i = 0, 1, 2, 3$. This procedure is equivalent to having twisted boundary conditions, such that the allowed momenta for the $\psi_{x,\uparrow}$ fermions are

$$\mathbf{k} = \frac{2\pi}{4L} (4j_x - n_y, 4j_y + n_x), \tag{A4}$$

where j_x, j_y are integers, thereby enhancing the momentum-space resolution of fermionic observables fourfold.

APPENDIX B: MAGNETIC CORRELATIONS FOR $\lambda = 1$ AND $\lambda = 2$, AND INSIDE THE SUPERCONDUCTING PHASE

In this appendix, we present additional data for the bosonic and fermionic SDW susceptibilities $\chi(\mathbf{q}, i\omega_n, r, T)$ and $S_{xx}(\mathbf{q}, i\omega_n, r, T)$. We begin with Fig. 18, which shows $\chi^{-1}(\mathbf{q} = \mathbf{Q}, i\omega_n = 0)$ across the phase diagrams for $\lambda = 1.5$ and $\lambda = 2$. It illustrates how the bending of the SDW finite-temperature transition line is also visible in χ^{-1} for $r > r_{c0}$, similarly to the behavior for $\lambda = 1$ in Fig. 3, where, however, no superconducting phase has been observed within our temperature resolution.

Next, to complement the discussion in Sec. III, where we have focused on the Yukawa coupling $\lambda = 1.5$ and a bosonic velocity of $c = 3$, we here show detailed data for values $\lambda = 1$

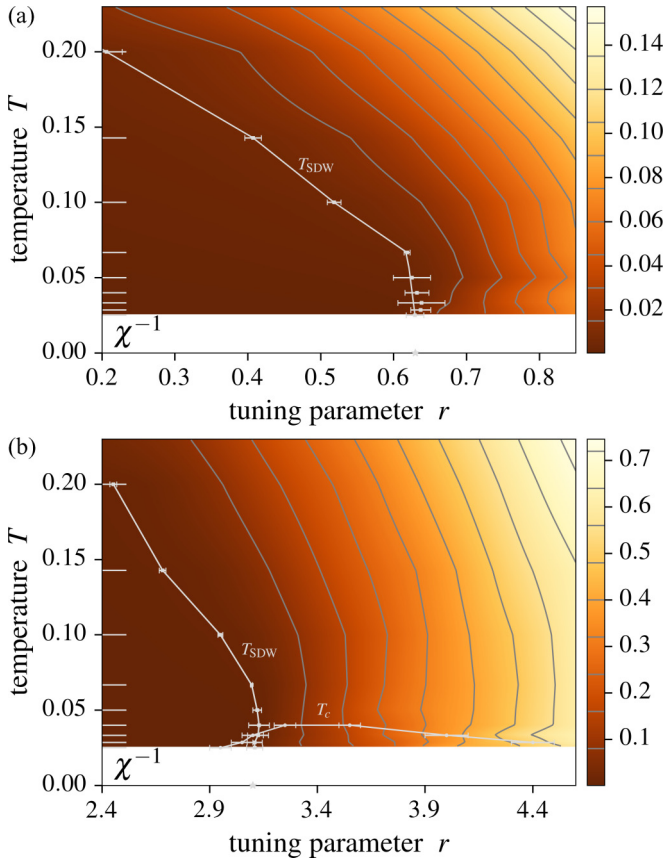
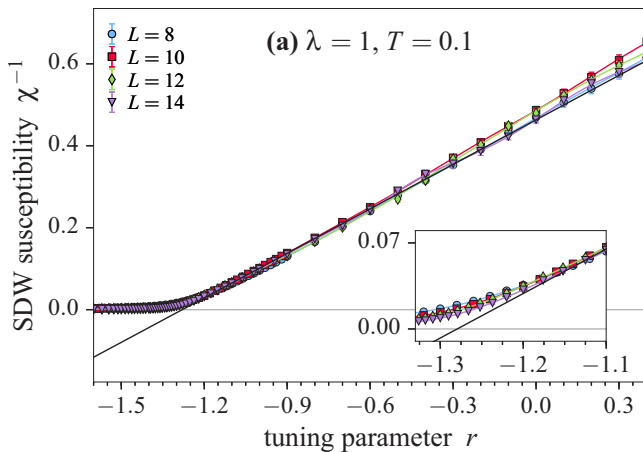


FIG. 18. Companion figure to Fig. 3 for (a) $\lambda = 1.5$ and (b) $\lambda = 2$.

and 2 at the same velocity c . In Fig. 19, we show $\chi^{-1}(\mathbf{q} = \mathbf{Q}, i\omega_n = 0)$ as a function of r for constant $T = 0.1$, where the same linear dependence as for $\lambda = 1$ (Fig. 6) is apparent. As we show in Fig. 20 both for $r \approx r_{c0}$ and a range of $r > r_{c0}$ the leading frequency dependence of χ^{-1} is clearly linear, similarly to $\lambda = 1.5$ (Fig. 7), whereas the leading momentum dependence shown in Fig. 21 is quadratic in $\mathbf{q} - \mathbf{Q}$, which is again comparable to $\lambda = 1.5$ (Fig. 8). Note that for $\lambda = 2$



we show data at a higher temperature $T = 1/20$ rather than at $T = 1/40$, because otherwise the system would be in the superconducting phase, where the frequency dependence is significantly altered. For small frequencies and momenta the fermionic susceptibility S_{xx}^{-1} in Fig. 22 behaves similarly to the bosonic χ^{-1} (see Fig. 9 for $\lambda = 1.5$).

The temperature dependence of both χ^{-1} and S_{xx}^{-1} is demonstrated in Fig. 23. As in the case of $\lambda = 1.5$ (Fig. 10), we observe a linear regime at high temperatures, shown in the insets, and a crossover region, where we can fit a quadratic law. For $\lambda = 1$, this second region extends down to lower temperatures than for $\lambda = 1.5$, where T_c is higher. At $\lambda = 2$, the data for $T < 0.05$ are from within the superconducting phase. Moreover, at $r = 3.1 \approx r_{c0}$ the system is partially inside the magnetic quasi-long-range order phase (cf. the phase diagram in Fig. 2).

Finally, to illustrate the influence of superconductivity on the frequency dependence of the SDW susceptibility, we show data from deep within the superconducting phase in Fig. 24. Here we have chosen a data set with different values of the Yukawa coupling $\lambda = 3$ and the bosonic velocity $c = 2$ (as in Ref. [28]) since $T_c^{\max} \approx 0.08$ is about twice as high for these parameters as for $\lambda = 2, c = 3$. In contrast to the data at $T > T_c$ shown in Figs. 7 and 20, the low-frequency behavior is clearly no longer purely linear—indicative of a suppression of Landau damping in the superconducting phase.

APPENDIX C: COMPARISON WITH A ONE LOOP APPROXIMATION FOR THE FERMION SELF-ENERGY

In this Appendix, we consider the fermionic self-energy in a one-loop approximation. To this order, the self-energy is given by

$$\Sigma_{\mathbf{k}, \alpha=y}(\omega_n) = \frac{\lambda^2}{\beta L^2} \sum_{\mathbf{q}, m} \chi_{\mathbf{q}}(\Omega_m) G_{\mathbf{k}+\mathbf{q}, \alpha=x}^0(\omega_n + \Omega_m), \quad (\text{C1})$$

where G^0 is the noninteracting Green's function and $\Omega_m = 2\pi mT$ is a bosonic Matsubara frequency. Deferring more systematic calculations for future work, here we do not attempt

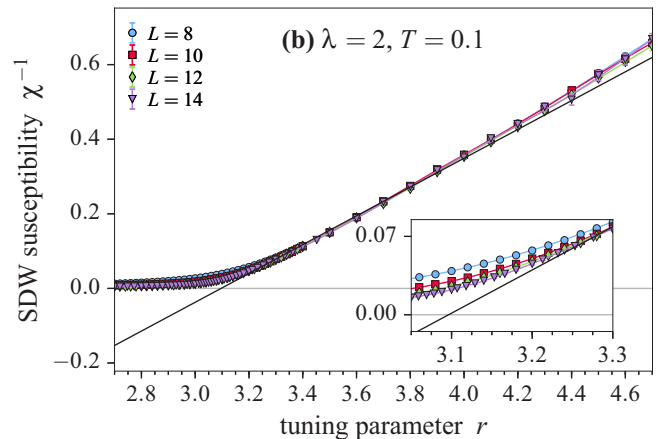
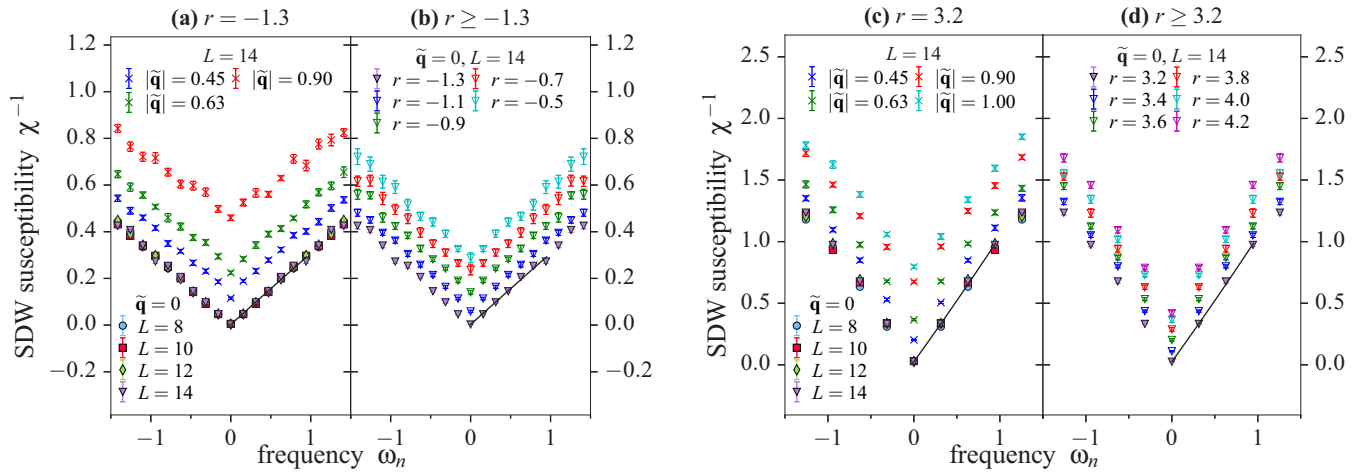


FIG. 19. Companion figure of Fig. 6 for Yukawa couplings (a) $\lambda = 1$ and (b) $\lambda = 2$. The black lines are linear fits of the $L = 14$ data for (a) $r > -1.2$ and (b) $r > 3.2$.


 FIG. 20. Companion figure of Fig. 7 for Yukawa couplings $\lambda = 1$ at $T = 1/40$ (left) and $\lambda = 2$ at $T = 1/20$ (right).

a full, self-consistent solution of the coupled Eliashberg equations [8] for the SDW correlations and the fermionic Green's function. Instead, we use the noninteracting Green's function and χ taken from a lattice, discretized imaginary time version of Eq. (4):

$$\chi_{\mathbf{q}}^{-1}(\Omega_m) = a_r(r - r_c) + 4a_q \left[\sin^2 \left(\frac{q_x - Q_x}{2} \right) + \sin^2 \left(\frac{q_y - Q_y}{2} \right) \right] + \frac{2a_\omega}{\Delta\tau} \left| \sin \left(\frac{\Delta\tau\Omega_m}{2} \right) \right|, \quad (\text{C2})$$

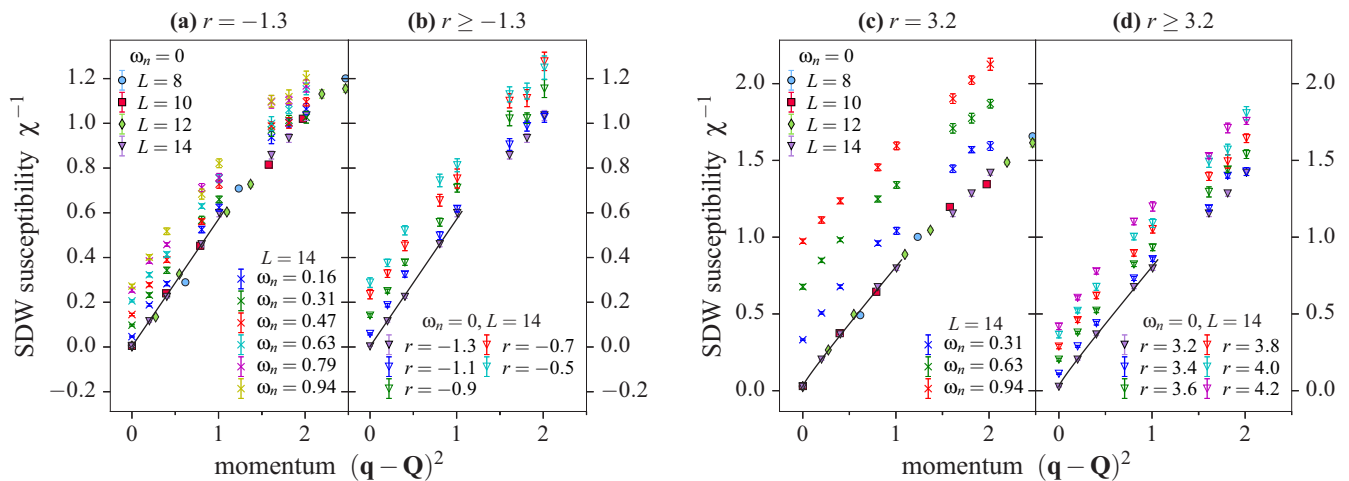
where the parameters a_r, a_q, a_ω are taken from a fit to the DQMC data, see Section III A. Strictly speaking, this procedure is not justified. However, since within a self-consistent Eliashberg theory, χ has the form (4, C2), we expect our simplified approximation to capture the general behavior of the self-consistent theory.

In Fig. 25, we show the imaginary part of the self-energy. The results bear some similarities to the DQMC data, shown in

Fig. 15. Whereas at moderate $r - r_c$ or away from the hotspots the self-energy is rapidly diminished as the frequency ω_n is lowered, the behavior at the hotspots as r approaches r_c is different. There, as a function of temperature, a change of slope occurs in the frequency dependence of the self-energy, where at intermediate temperatures $T \approx 0.1$ the self-energy is nearly frequency independent. Only at lower temperatures, $\Sigma_{\mathbf{k}_{hs}}(\omega_n)$ starts resembling the expected $\sqrt{(\omega_n)}$ form. In comparing with the DQMC results in Fig. 15, we note the similar magnitude of the self-energy. However, the DQMC results show a far weaker temperature dependence at the hotspots for r close to r_c .

APPENDIX D: EXTRACTING THE SUPERCONDUCTING GAP

In this appendix, we provide a detailed description of the procedure by which we extract the single-particle excitation energy $E_{\mathbf{k}}$ in the superconducting state, which we discuss in Sec. V of the main text. The single-particle Green's function


 FIG. 21. Companion figure of Fig. 8 for Yukawa couplings $\lambda = 1$ at $T = 1/40$ (left) and $\lambda = 2$ at $T = 1/20$ (right).

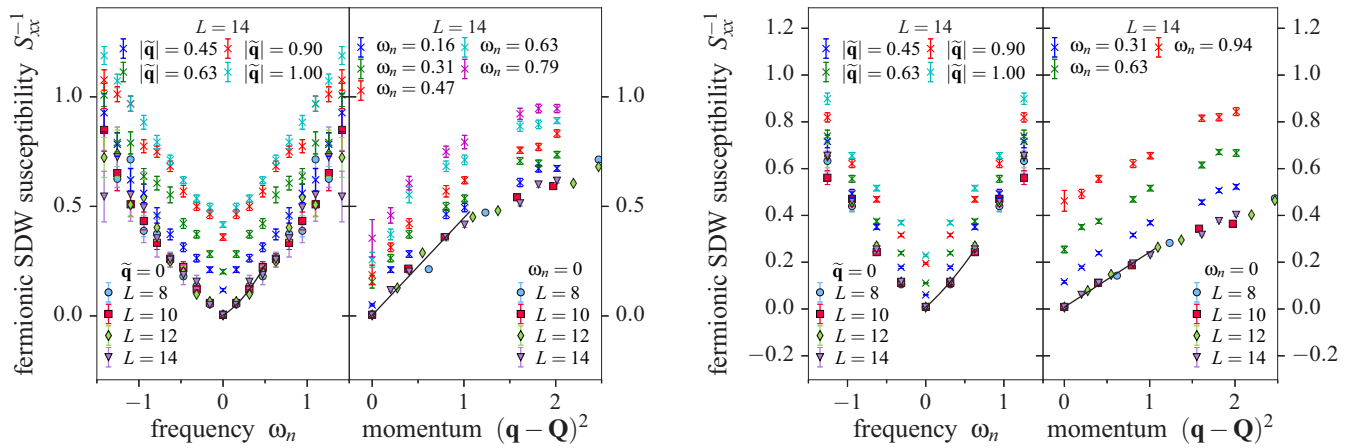


FIG. 22. Companion figure of Fig. 9 for Yukawa couplings $\lambda = 1$ at $T = 1/40$ (left) and $\lambda = 2$ at $T = 1/20$ (right).

$G_{\mathbf{k}}(\tau)$ is found to exhibit a characteristic imaginary-time evolution as shown in Fig. 26. At intermediate times, $\tau_0 < \tau < \beta/2$, where $\tau_0 \sim 1$ is some microscopic time scale, the single-particle Green's function decays exponentially as

$$G_{\mathbf{k}}(\tau) \propto e^{-E_{\mathbf{k}}^p \tau}, \quad (\text{D1})$$

and similarly, for times $\tau_0 < \beta - \tau < \beta/2$,

$$G_{\mathbf{k}}(\tau) \propto e^{-E_{\mathbf{k}}^h(\beta-\tau)}. \quad (\text{D2})$$

At long times, $\tau \approx \beta/2$ the Green's function is substantially suppressed and statistical errors dominate the signal. We extract the decay constants $E_{\mathbf{k}}^p$ and $E_{\mathbf{k}}^h$ from appropriate

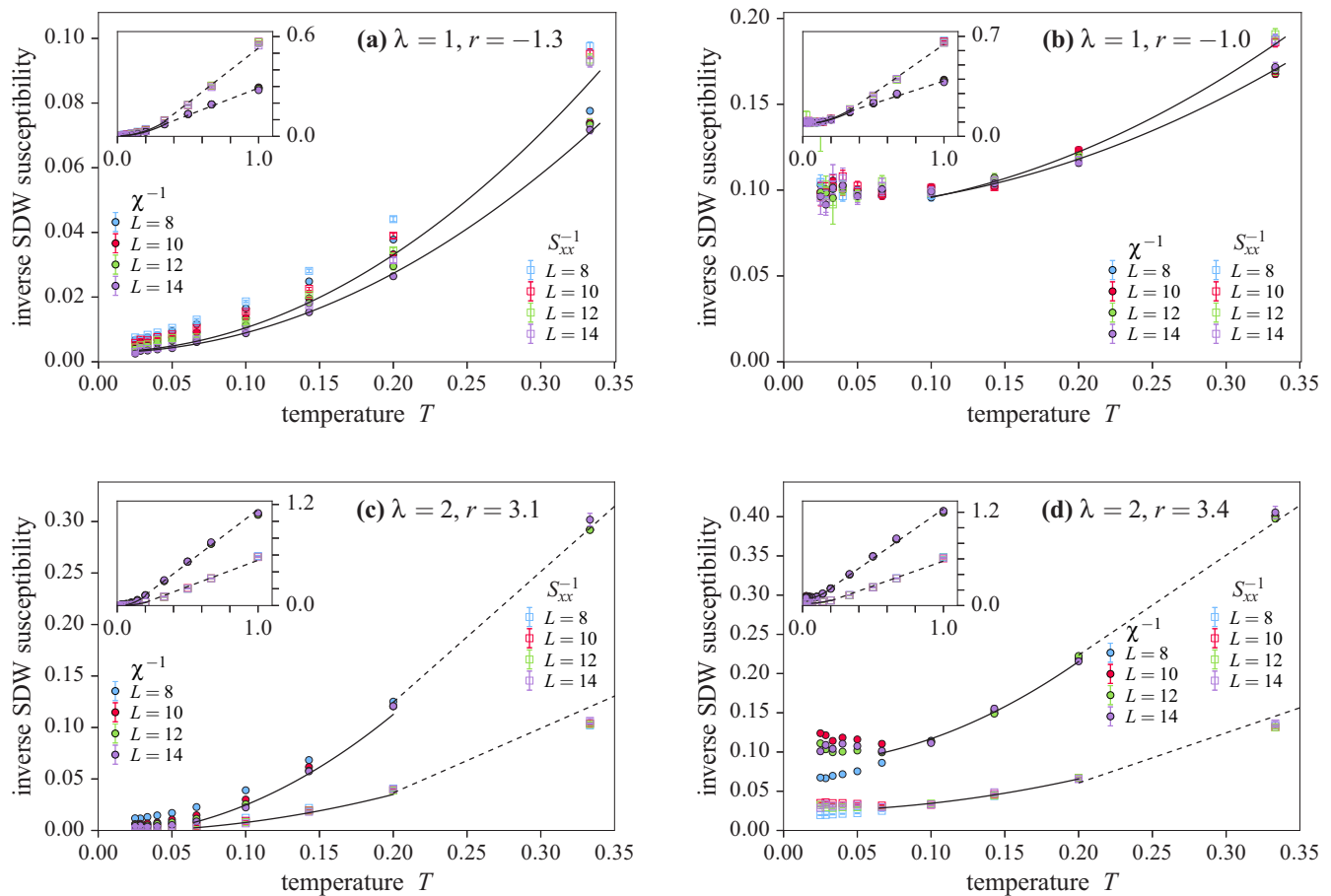


FIG. 23. Companion figure of Fig. 10 for for (top) $\lambda = 1$ at (a) $r = -1.3 \approx r_{c0}$ and at (b) $r = -1.0 > r_{c0}$, and for (bottom) $\lambda = 2$ at (c) $r = 3.1 \approx r_{c0}$ and at (d) $r = 3.4 > r_{c0}$.

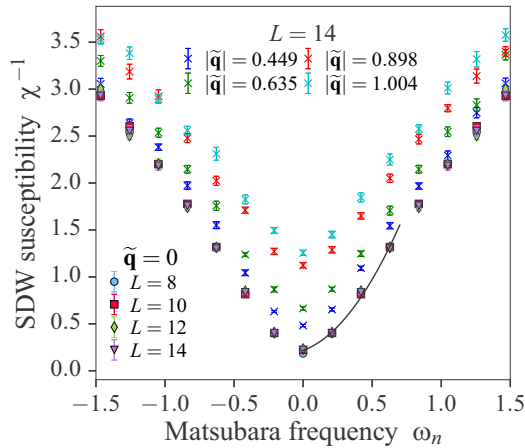


FIG. 24. Frequency dependence of the SDW susceptibility χ^{-1} for $\lambda = 3$, $c = 2$ at $T = 1/30 < T_c$ and $r = 10.37 \approx r_{\text{opt}}$, close to where T_c is highest for this set of parameters, shown for various momenta $\mathbf{q} = \mathbf{Q} + \tilde{\mathbf{q}}$. The black line is the best fit of a second degree polynomial $b_0 + b_1|\omega_n| + b_2\omega_n^2$ to the $\mathbf{q} = \mathbf{Q}$, $L = 14$ low-frequency data.

exponential fits and define the single-particle excitation energy as their minimum $E_{\mathbf{k}} = \min\{E_{\mathbf{k}}^p, E_{\mathbf{k}}^h\}$.

For a qualitative understanding of these results, we consider the behavior of the Green's function in a Fermi liquid and in a Bardeen-Cooper-Schrieffer (BCS) superconductor. The fact that $G_{\mathbf{k}}(\tau)$ exhibits exponential behavior can be interpreted as arising from a peak in the spectral function $A_{\mathbf{k}}(\omega)$, occurring at a nonzero frequency, as can be seen from (7). In a Fermi liquid, the spectral function at a given momentum has a single, sharp peak at the energy of the quasiparticle. It then follows that $G_{\mathbf{k}}(\tau)$ has the form of a single exponential, with holelike quasiparticles obeying (D2) and particlelike

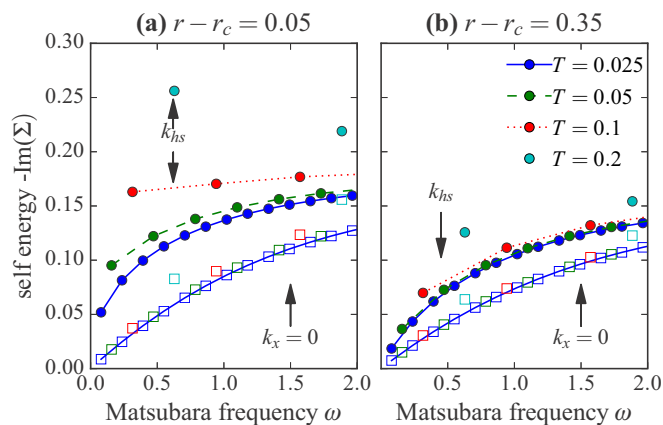


FIG. 25. Imaginary part of the self-energy (C1), calculated within a one-loop approximation for several temperatures for two momenta on the Fermi surface and (a) close to the QCP at $r = r_c + 0.05$, (b) further away from the QCP. An SDW correlator of the form (C2) was used, with the parameters taken from the fit to the DQMC data for $\lambda = 1.5$, $c = 3$, with $\Delta\tau = 0.1$, and $L = 200$, as shown in Fig. 5(b). The data for $\mathbf{k} = \mathbf{k}_{hs}$ are indicated by full circles, the momentum away from the hot spot is indicated by empty squares.

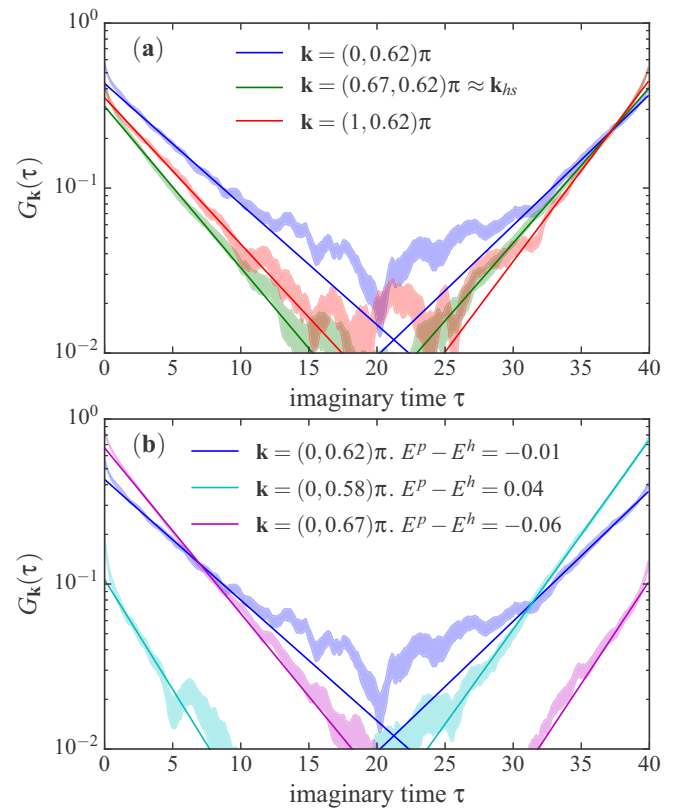


FIG. 26. Imaginary time evolution of the single-particle Green's function $G_{\mathbf{k}}(\tau)$ for (a) several momenta along the noninteracting Fermi surface and (b) several momenta along a cut perpendicular to the Fermi surface. Here, $L = 12$, $T = 1/40$, $\lambda = 3$, and $c = 2$. Shaded regions indicate the statistical uncertainty. The solid lines are exponential fits.

quasiparticles obeying (D1). Indeed, in our simulations in the normal state we find monotonic behavior of $G_{\mathbf{k}}(\tau)$ (not shown). It is illuminating to contrast this behavior with the BCS state, where a superposition of holelike and particlelike excitations is allowed. In this case, the spectral function consists of two delta-function peaks at $\omega = \pm E_{\mathbf{k}}$, such that the Green's function takes the form

$$G_{\mathbf{k}}(\tau) = \frac{1}{1 + e^{-\beta E_{\mathbf{k}}}} (u_{\mathbf{k}}^2 e^{-E_{\mathbf{k}}\tau} + v_{\mathbf{k}}^2 e^{-E_{\mathbf{k}}(\beta - \tau)}). \quad (\text{D3})$$

Here, $E_{\mathbf{k}} = \sqrt{\Delta_{\mathbf{k}}^2 + \epsilon_{\mathbf{k}}^2}$ with the quasiparticle dispersion $\epsilon_{\mathbf{k}}$ and the gap $\Delta_{\mathbf{k}}$, and $u_{\mathbf{k}}$, $v_{\mathbf{k}}$ are particle and hole amplitudes, respectively. The resulting Green's function is nonmonotonic, showing a minimum at a finite imaginary time.

While our numerical data below T_c share some similarities with the BCS form (D3), they differ in two notable ways. First, clear exponential behavior is not seen at short times $\tau \lesssim \tau_0 \sim 1$. Second, the particle and hole excitation energies differ, i.e., $E_{\mathbf{k}}^p \neq E_{\mathbf{k}}^h$, with the difference more pronounced away from the Fermi surface, as illustrated in Fig. 26(b).

- [1] N. P. Armitage, P. Fournier, and R. L. Greene, Progress and perspectives on electron-doped cuprates, *Rev. Mod. Phys.* **82**, 2421 (2010).
- [2] J. Paglione and R. L. Greene, High-temperature superconductivity in iron-based materials, *Nat. Phys.* **6**, 645 (2010).
- [3] P. Gegenwart, Q. Si, and F. Steglich, Quantum criticality in heavy-fermion metals, *Nat. Phys.* **4**, 186 (2008).
- [4] S. Brown, Organic superconductors: The Bechgaard salts and relatives, *Physica C: Superconductivity and its Applications* **514**, 279 (2015).
- [5] J. A. Hertz, Quantum critical phenomena, *Phys. Rev. B* **14**, 1165 (1976).
- [6] A. J. Millis, Effect of a nonzero temperature on quantum critical points in itinerant fermion systems, *Phys. Rev. B* **48**, 7183 (1993).
- [7] A. Abanov and A. Chubukov, Spin-Fermion Model Near the Quantum Critical Point: One-Loop Renormalization Group Results, *Phys. Rev. Lett.* **84**, 5608 (2000).
- [8] A. Abanov, A. Chubukov, and J. Schmalian, Quantum-critical theory of the spin-fermion model and its application to cuprates: Normal state analysis, *Adv. Phys.* **52**, 119 (2003).
- [9] A. Abanov and A. Chubukov, Anomalous Scaling at the Quantum Critical Point in Itinerant Antiferromagnets, *Phys. Rev. Lett.* **93**, 255702 (2004).
- [10] J. Rech, C. Pépin, and A. V. Chubukov, Quantum critical behavior in itinerant electron systems: Eliashberg theory and instability of a ferromagnetic quantum critical point, *Phys. Rev. B* **74**, 195126 (2006).
- [11] H. V. Löhneysen, A. Rosch, M. Vojta, and P. Wölfle, Fermi-liquid instabilities at magnetic quantum phase transitions, *Rev. Mod. Phys.* **79**, 1015 (2007).
- [12] S.-S. Lee, Low-energy effective theory of Fermi surface coupled with U(1) gauge field in 2 + 1 dimensions, *Phys. Rev. B* **80**, 165102 (2009).
- [13] D. F. Mross, J. McGreevy, H. Liu, and T. Senthil, Controlled expansion for certain non-Fermi-liquid metals, *Phys. Rev. B* **82**, 045121 (2010).
- [14] M. A. Metlitski and S. Sachdev, Quantum phase transitions of metals in two spatial dimensions. I. Ising-nematic order, *Phys. Rev. B* **82**, 075127 (2010).
- [15] M. A. Metlitski and S. Sachdev, Quantum phase transitions of metals in two spatial dimensions. II. Spin density wave order, *Phys. Rev. B* **82**, 075128 (2010).
- [16] S. A. Hartnoll, D. M. Hofman, M. A. Metlitski, and S. Sachdev, Quantum critical response at the onset of spin-density-wave order in two-dimensional metals, *Phys. Rev. B* **84**, 125115 (2011).
- [17] E. Berg, M. A. Metlitski, and S. Sachdev, Sign-problem-free quantum Monte Carlo of the onset of antiferromagnetism in metals, *Science* **338**, 1606 (2012).
- [18] D. Dalidovich and S.-S. Lee, Perturbative non-Fermi liquids from dimensional regularization, *Phys. Rev. B* **88**, 245106 (2013).
- [19] K. B. Efetov, H. Meier, and C. Pepin, Pseudogap state near a quantum critical point, *Nat. Phys.* **9**, 442 (2013).
- [20] J. Lee, P. Strack, and S. Sachdev, Quantum criticality of reconstructing Fermi surfaces in antiferromagnetic metals, *Phys. Rev. B* **87**, 045104 (2013).
- [21] V. S. de Carvalho and H. Freire, Breakdown of Fermi liquid behavior near the hot spots in a two-dimensional model: A two-loop renormalization group analysis, *Nucl. Phys. B* **875**, 738 (2013).
- [22] A. L. Fitzpatrick, S. Kachru, J. Kaplan, and S. Raghu, Non-Fermi-liquid behavior of large- N_B quantum critical metals, *Phys. Rev. B* **89**, 165114 (2014).
- [23] T. Holder and W. Metzner, Anomalous dynamical scaling from nematic and U(1) gauge field fluctuations in two-dimensional metals, *Phys. Rev. B* **92**, 041112(R) (2015).
- [24] S. Raghu, G. Torroba, and H. Wang, Metallic quantum critical points with finite BCS couplings, *Phys. Rev. B* **92**, 205104 (2015).
- [25] C. M. Varma, Quantum Criticality in Quasi-Two-Dimensional Itinerant Antiferromagnets, *Phys. Rev. Lett.* **115**, 186405 (2015).
- [26] C. M. Varma, L. Zhu, and A. Schröder, Quantum critical response function in quasi-two-dimensional itinerant antiferromagnets, *Phys. Rev. B* **92**, 155150 (2015).
- [27] S. A. Maier and P. Strack, Universality in antiferromagnetic strange metals, *Phys. Rev. B* **93**, 165114 (2016).
- [28] Y. Schattner, M. H. Gerlach, S. Trebst, and E. Berg, Competing Orders in a Nearly Antiferromagnetic Metal, *Phys. Rev. Lett.* **117**, 097002 (2016).
- [29] A. Schrief, P. Lunts, and S.-S. Lee, Exact critical exponents for the antiferromagnetic quantum critical metal in two dimensions, [arXiv:1608.06927](https://arxiv.org/abs/1608.06927).
- [30] M. A. Metlitski, D. F. Mross, S. Sachdev, and T. Senthil, Cooper pairing in non-Fermi liquids, *Phys. Rev. B* **91**, 115111 (2015).
- [31] R. Blankenbecler, D. J. Scalapino, and R. L. Sugar, Monte Carlo calculations of coupled boson-fermion systems. I, *Phys. Rev. D* **24**, 2278 (1981).
- [32] S. R. White, D. J. Scalapino, R. L. Sugar, E. Y. Loh, J. E. Gubernatis, and R. T. Scalettar, Numerical study of the two-dimensional Hubbard model, *Phys. Rev. B* **40**, 506 (1989).
- [33] E. Loh Jr. and J. E. Gubernatis, Stable numerical simulations of models of interacting electrons in condensed-matter physics, in *Electron. Phase Transitions*, edited by W. Hanke and Y. Kopayev, Modern Problems in Condensed Matter Sciences Vol. 10 (North Holland, Amsterdam, 1992), Chap. 4.
- [34] F. Assaad and H. Evertz, World-line and determinantal quantum Monte Carlo methods for spins, phonons and electrons, in *Computational Many-Particle Physics*, edited by H. Fehske, R. Schneider, and A. Weiße, Lecture Notes in Physics Vol. 739 (Springer, Berlin, 2008), pp. 277–356.
- [35] J. Gubernatis, N. Kawashima, and P. Werner, *Quantum Monte Carlo Methods: Algorithms for Lattice Models* (Cambridge University Press, Cambridge, UK, 2016).
- [36] Z.-X. Li, F. Wang, H. Yao, and D.-H. Lee, The nature of effective interaction in cuprate superconductors: A sign-problem-free quantum Monte-Carlo study, [arXiv:1512.04541](https://arxiv.org/abs/1512.04541).
- [37] S. Sachdev, *Quantum Phase Transitions*, 2nd ed. (Cambridge University Press, Cambridge, UK, 2011).
- [38] K. Hukushima and K. Nemoto, Exchange Monte Carlo method and application to spin glass simulations, *J. Phys. Soc. Jpn.* **65**, 1604 (1996).
- [39] H. G. Katzgraber, S. Trebst, D. A. Huse, and M. Troyer, Feedback-optimized parallel tempering Monte Carlo, *J. Stat. Mech. Theor. Exp.* (2006) P03018.
- [40] F. F. Assaad, Depleted Kondo lattices: Quantum Monte Carlo and mean-field calculations, *Phys. Rev. B* **65**, 115104 (2002).

- [41] Y. Schattner, S. Lederer, S. A. Kivelson, and E. Berg, Ising Nematic Quantum Critical Point in a Metal: A Monte Carlo Study, *Phys. Rev. X* **6**, 031028 (2016).
- [42] E. G. Moon and S. Sachdev, Quantum critical point shifts under superconductivity: Pnictides and cuprates, *Phys. Rev. B* **82**, 104516 (2010).
- [43] X. Wang, Y. Schattner, E. Berg, and R. M. Fernandes, [arXiv:1609.09568](https://arxiv.org/abs/1609.09568).
- [44] N. Trivedi and M. Randeria, Deviations from Fermi-Liquid Behavior Above T_c in 2D Short Coherence Length Superconductors, *Phys. Rev. Lett.* **75**, 312 (1995).
- [45] See e.g., Eduardo Fradkin, *Field Theories of Condensed Matter Physics* (Cambridge University Press, Cambridge, UK, 2013).
- [46] H. Matsui, K. Terashima, T. Sato, T. Takahashi, M. Fujita, and K. Yamada, Direct Observation of a Nonmonotonic $d_{x^2-y^2}$ -Wave Superconducting Gap in the Electron-Doped High- T_c Superconductor $\text{Pr}_{0.89}\text{LaCe}_{0.11}\text{CuO}_4$, *Phys. Rev. Lett.* **95**, 017003 (2005).
- [47] A. Abanov, A. V. Chubukov, and M. R. Norman, Gap anisotropy and universal pairing scale in a spin-fluctuation model of cuprate superconductors, *Phys. Rev. B* **78**, 220507(R) (2008).
- [48] S. Lederer, Y. Schattner, E. Berg, and S. A. Kivelson, [arXiv:1612.01542](https://arxiv.org/abs/1612.01542).
- [49] N. P. Armitage, D. H. Lu, C. Kim, A. Damascelli, K. M. Shen, F. Ronning, D. L. Feng, P. Bogdanov, Z.-X. Shen, Y. Onose, Y. Taguchi, Y. Tokura, P. K. Mang, N. Kaneko, and M. Greven, Anomalous Electronic Structure and Pseudogap Effects in $\text{Nd}_{1.85}\text{Ce}_{0.15}\text{CuO}_4$, *Phys. Rev. Lett.* **87**, 147003 (2001).
- [50] D. L. Maslov and A. V. Chubukov, Optical response of correlated electron systems, [arXiv:1608.02514](https://arxiv.org/abs/1608.02514).
- [51] Y. Schattner *et al.* (unpublished).
- [52] C. Wu and S.-C. Zhang, Sufficient condition for absence of the sign problem in the fermionic quantum Monte Carlo algorithm, *Phys. Rev. B* **71**, 155115 (2005).
- [53] Z. C. Wei, C. Wu, Y. Li, S. Zhang, and T. Xiang, Majorana Positivity and the Fermion Sign Problem of Quantum Monte Carlo Simulations, *Phys. Rev. Lett.* **116**, 250601 (2016).
- [54] Z.-X. Li, Y.-F. Jiang, and H. Yao, Majorana-time-reversal symmetries: a fundamental principle for sign-problem-free quantum Monte Carlo simulations, [arXiv:1601.05780](https://arxiv.org/abs/1601.05780) [cond-mat.str-el].